

Cross-modal linkage risk in clinical vision-language models

Soroosh Tayebi Arasteh^{1,2*}, Mahshad Lotfinia^{1,2}, Sven Nebelung^{1,2}, and Daniel Truhn^{1,2}

¹ Lab for AI in Medicine, RWTH Aachen University, Aachen, Germany

² Department of Diagnostic and Interventional Radiology, University Hospital RWTH Aachen, Aachen, Germany

*Correspondence to: Soroosh Tayebi Arasteh (soroosh.arasteh@rwth-aachen.de)

Abstract. Vision-language models (VLMs) trained on paired chest radiographs and radiology reports learn a shared embedding space that can preserve instance-level image-report correspondence. This poses a privacy risk in settings where radiographs and reports are deliberately kept separate after acquisition, such as image-only data sharing or access-controlled reports, because a de-identified image may be re-linked to its original narrative report through cosine similarity alone. We formalized this as image-to-report retrieval and used public paired cohorts, in which the true pairing is known by design, as ground-truth benchmarks to audit the risk rather than as the privacy scenario. Evaluating VLMs of increasing clinical specialization on 406,241 paired examples from 126,804 patients across MIMIC-CXR (43,793 held-out pairs) and external CheXpert Plus (29,296 pairs), we found that re-linkage rose systematically with specialization: the strongest VLM retrieved the correct report at 15 times chance at a candidate pool of $N = 100$, 50 times chance at $N = 10,000$, and well above chance at full-database scale. The signal persisted under pathology-matched hard negatives that removed disease-label shortcuts, indicating correspondence beyond broad diagnostic categories. To reduce it without retraining, we froze both encoders and applied differentially private optimization only to the projection heads defining the alignment layer ($\epsilon = 0.34$, $\delta = 6 \times 10^{-6}$). This reduced Recall@1 by 61.8% at $N = 10,000$ on MIMIC-CXR and transferred to CheXpert Plus without retraining, while image-side utility was largely preserved: macro AUROC for linear-probe classification across 14 labels shifted only from 79.63% to 79.43%. Targeted differentially private finetuning of the shared alignment layer can substantially reduce cross-modal re-linkage without materially degrading the image representations that make these models clinically useful.

Introduction

Clinical artificial intelligence (AI) is increasingly built around vision-language models (VLMs) trained on paired medical images and free-text reports [1,2]. In chest radiography, this paradigm is especially attractive because chest radiographs and radiology reports are naturally paired at scale, allowing multimodal models to learn shared representations that support retrieval, representation learning, report generation, and zero-shot transfer [3,4,5,6]. Yet the same alignment that makes these models useful may also create a privacy vulnerability that is easy to overlook. If a chest radiograph and its report remain close in the shared embedding space, then a de-identified image may still be reconnectable to the report with which it was originally paired through similarity search alone. In radiology, that possibility is especially consequential because the report contains substantially richer and more specific information than a disease label, often including comparisons, qualifiers, technical context, and narrative findings that extend well beyond what is visible in a simple categorical annotation [7,8].

This raises a privacy question that is distinct from standard de-identification and distinct from the image-only privacy attacks more commonly studied in medical AI [9,10]. Prior work has focused mainly on settings such as membership inference, reconstruction risk, or classification under

differential privacy (DP) [11,12,13,14]. Those lines of work are important, but they do not directly address cross-modal re-association in clinical VLMs. In multimodal radiology models [15], the central learned object is not only an image representation or a text representation in isolation, but the alignment between them [4,5,6]. That alignment may preserve instance-level correspondence beyond broad pathology labels, making it possible to recover a paired report not merely because it describes edema, pleural effusion, or no finding, but because the model has learned a sharper image-report binding [16]. This matters in practice because public multimodal checkpoints are increasingly downloaded, reused, and adapted on clinical data, whereas the privacy assumptions attached to de-identified datasets were not designed with shared cross-modal embedding spaces in mind [1,17].

An important clarification concerns what these public datasets represent in this study. In resources such as MIMIC-CXR and CheXpert Plus the image-report pairing is intentionally published, so recovering a report from its radiograph within these datasets is not in itself a privacy breach. We therefore use them not as the privacy scenario but as ground-truth benchmarks: because the true pairing is known, they allow us to audit whether a model’s shared embedding space preserves enough instance-level structure to make reports recoverable from images. The deployment settings this audit speaks to are those in which radiographs and reports are deliberately held distinct after acquisition, including image-only data sharing, separate access control for narrative reports, institutional data enclaves, and vendor or model evaluation pipelines, as well as downstream releases where reports are not meant to be recoverable from image embeddings. In such settings, a VLM’s shared embedding space may weaken that intended separation by preserving pairwise image-report structure, and the benchmarks used here quantify how strongly a given model does so.

Here we address that gap by formalizing cross-modal linkage risk as an image-to-report retrieval problem (see Fig. 1). We ask whether a held-out chest radiograph can retrieve its true paired report from a candidate pool, how that risk changes as the candidate pool grows, and whether the signal persists when distractor reports are chosen to be clinically similar rather than random [5,6,18]. To answer those questions, we evaluate four publicly available VLMs spanning increasing levels of domain specialization, from general-domain CLIP [19] to the radiology-specific BioViL-T [6]. We study retrieval on two large public chest radiograph resources: a held-out MIMIC-CXR test set [3], which is a large public hospital chest radiograph dataset comprising 43,793 image-report pairs in our evaluation split, and an external CheXpert Plus test set [20], which pairs the public CheXpert [21] chest radiograph benchmark with its corresponding report resource and comprises 29,296 image-report pairs in our external evaluation split. We then test a practical mitigation strategy that targets the final shared alignment layer rather than the full multimodal backbone, using head-only differentially private finetuning while keeping the image and text encoders frozen. A non-private entropy-regularized [22] alternative is included as a comparator. To determine whether reducing linkage comes at the cost of clinically meaningful image information [23], we evaluate post-mitigation image embeddings on 14 chest radiograph abnormality tasks, spanning atelectasis, cardiomegaly, consolidation, edema, enlarged cardiomeastinum, fracture, lung lesion, lung opacity, no finding, pleural effusion, pleural other, pneumonia, pneumothorax, and support devices.

Our starting assumption is that linkage risk should increase with clinical specialization, because models trained closer to the chest radiograph reporting distribution are more likely to preserve sharper image-report correspondence [4,5,24,6]. We further expect that if the signal reflects genuine instance-level binding rather than only broad disease similarity, it should remain detectable at database scale and under pathology-matched hard negatives, even if attenuated. Finally, because the retrieval risk is mediated directly by the space in which images and reports are brought together, we expect the final projection heads to be a tractable intervention point for privacy-aware mitigation [19,6,16]. Under that framing, this study treats multimodal alignment in clinical

foundation models as both a capability and a liability [13]. The aim is not only to show that cross-modal re-linkage is measurable in off-the-shelf clinical VLMs, but also to test whether that risk can be reduced in a practical way without materially sacrificing image-side diagnostic utility. More broadly, the work argues that responsible evaluation of clinical multimodal models must account not only for what shared embeddings enable, but also for what they may unintentionally reconnect [25,13].

Results

Off-the-shelf clinical VLMs enable cross-modal re-linkage

The starting point was to test whether a publicly available VLM can reconnect a held-out chest radiograph to the report with which it was originally paired using only similarity in a shared image-text embedding space. We evaluated image-to-report retrieval on two paired cohorts, namely a held-out MIMIC-CXR test set comprising 43,793 image-report pairs and an external CheXpert Plus test set comprising 29,296 pairs. For each query radiograph, candidate reports were ranked by cosine similarity in the shared embedding space, and retrieval performance was summarized primarily by Recall@1, with Recall@5, Recall@10, and mean reciprocal rank (MRR) reported as complementary metrics. Four off-the-shelf models were compared, spanning increasing domain specialization from general-domain CLIP to the radiology-specific BioViL-T. The overall pattern across datasets and candidate-pool sizes is shown in Fig. 2, and the main random-candidate retrieval results are summarized in Table 1, while exhaustive results for all models and candidate-pool sizes, including 95% confidence intervals, are provided in Supplementary Tables 1 and 2.

A comparison at $N = 100$ candidate reports already revealed a clear hierarchy of linkage strength. On MIMIC-CXR, BioViL-T achieved a Recall@1 of $15.440\% \pm 0.141$, compared with $5.829\% \pm 0.091$ for BiomedCLIP [24], $1.594\% \pm 0.046$ for PubMedCLIP [26], and $1.203\% \pm 0.035$ for CLIP (Table 1). The same ordering was reflected in Recall@5, Recall@10, and MRR, indicating that the radiology-specialized model was not only more likely to retrieve the correct report at rank one, but also more likely to keep it near the top of the candidate list more generally. Because chance Recall@1 at $N = 100$ is 1.000%, these values show that off-the-shelf multimodal embeddings can already recover the true paired report at rates well above random matching, with the effect increasing sharply as the model becomes more specialized for medical and radiological data.

The external CheXpert Plus test set showed the same qualitative ordering, although with a weaker absolute signal and a narrower separation between the two strongest medical models. At $N = 100$, BioViL-T reached a Recall@1 of $7.281\% \pm 0.114$, compared with $5.456\% \pm 0.100$ for BiomedCLIP, $1.179\% \pm 0.047$ for PubMedCLIP, and $0.928\% \pm 0.040$ for CLIP (Table 1). Cross-modal re-linkage was therefore not confined to the internal evaluation cohort, but remained detectable under external transfer [27], again with the strongest signal arising in the model most closely aligned with chest radiology. Taken together, these results show that off-the-shelf clinical VLMs can re-link de-identified chest radiographs to their paired reports, and that the strength of this linkage tracks the degree of domain specialization of the underlying multimodal model.

Linkage remains above chance at database scale and under hard negatives

A more demanding evaluation reduced retrieval performance, but did not eliminate the linkage signal. To test whether the observed re-linkage survived under more stringent conditions, candidate pools were expanded from $N = 100$ to $N = 1,000$, $N = 10,000$, and the full test set, and a separate hard-negative protocol replaced random distractors with pathology-matched reports. The scaling

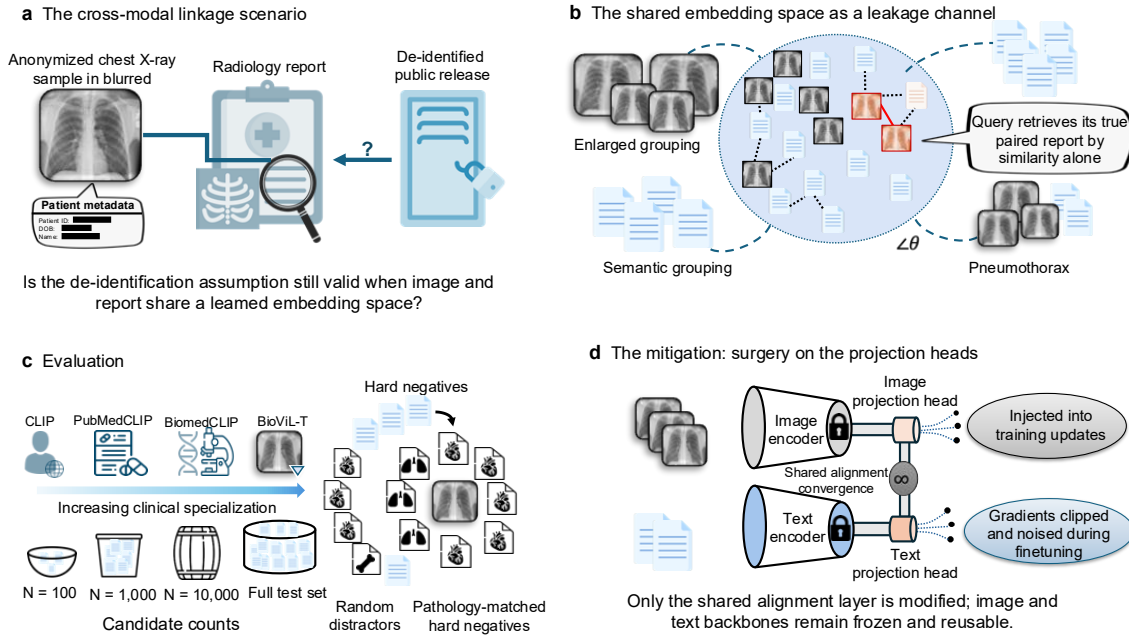


Fig. 1: Cross-modal linkage risk in clinical vision-language models (VLMs) and mitigation strategy. This schematic outlines the mechanism of the linkage vulnerability, our systematic evaluation framework, and the targeted privacy-preserving intervention. **a** When radiographs and reports are kept separate after acquisition, standard de-identification removes explicit metadata from the image but does not prevent the shared embedding space of a clinical VLM from re-linking it to its original, information-rich narrative report. **b** In the joint multi-modal manifold, images and reports are aligned by angular similarity ($\angle\theta$). Aggressive alignment during pretraining preserves instance-level correspondence, allowing a query CXR to retrieve its true paired report from a database. **c** We assessed the vulnerability across four models with increasing clinical specialization (CLIP, PubMedCLIP, BiomedCLIP, and BioViL-T) and quantified as the candidate-pool size scales to database levels. The signal is further tested under pathology-matched hard negatives to isolate instance-level binding from broad disease similarity. **d** To reduce linkage while preserving utility, the image and text backbones are frozen, and only the shared alignment layers (projection heads) are finetuned. Differentially private (DP) optimization is used to noise the alignment updates.

Table 1: Setting A. Cross-modal retrieval performance of off-the-shelf vision-language models on the MIMIC-CXR and CheXpert Plus test sets under the random-candidate protocol. For each query chest radiograph, the paired radiology report is retrieved from a candidate pool sampled from the held-out test split. Performance is evaluated using Recall@1, Recall@5, Recall@10, and mean reciprocal rank (MRR). Values are reported in percent as mean \pm standard deviation. For compact presentation, all four models are shown at $N = 100$, whereas larger candidate pools focus on the two strongest medically adapted models; exhaustive results for all models and candidate-pool sizes, including 95% confidence intervals, are provided in Supplementary Tables 1 and 2.

Dataset	N	Model	Recall@1	Recall@5	Recall@10	MRR
MIMIC-CXR	100	BioViL-T	15.440 \pm 0.141	41.896 \pm 0.223	58.673 \pm 0.225	28.936 \pm 0.152
		BiomedCLIP	5.829 \pm 0.091	19.987 \pm 0.173	31.709 \pm 0.203	14.523 \pm 0.109
		PubMedCLIP	1.594 \pm 0.046	6.316 \pm 0.104	11.787 \pm 0.140	6.113 \pm 0.062
		CLIP	1.203 \pm 0.035	5.917 \pm 0.092	11.346 \pm 0.127	5.674 \pm 0.052
	1,000	Random	1.000 \pm 0.000	5.000 \pm 0.000	10.000 \pm 0.000	5.187 \pm 0.000
		BioViL-T	3.320 \pm 0.065	11.197 \pm 0.140	17.723 \pm 0.180	8.407 \pm 0.087
		BiomedCLIP	0.997 \pm 0.039	3.772 \pm 0.086	6.330 \pm 0.114	3.235 \pm 0.054
		BioViL-T	0.496 \pm 0.027	2.040 \pm 0.060	3.642 \pm 0.083	1.790 \pm 0.037
	10,000	BiomedCLIP	0.137 \pm 0.015	0.613 \pm 0.035	1.118 \pm 0.051	0.604 \pm 0.021
		BioViL-T	0.150 \pm 0.019	0.570 \pm 0.036	1.037 \pm 0.049	0.602 \pm 0.022
	43,793	BioViL-T	0.150 \pm 0.019	0.570 \pm 0.036	1.037 \pm 0.049	0.602 \pm 0.022
		BiomedCLIP	0.041 \pm 0.010	0.167 \pm 0.020	0.281 \pm 0.026	0.191 \pm 0.012
CheXpert Plus	100	BioViL-T	7.281 \pm 0.114	25.063 \pm 0.220	39.423 \pm 0.256	17.628 \pm 0.136
		BiomedCLIP	5.456 \pm 0.100	18.270 \pm 0.196	29.478 \pm 0.234	13.684 \pm 0.123
		PubMedCLIP	1.179 \pm 0.047	5.784 \pm 0.123	11.425 \pm 0.172	5.715 \pm 0.069
		CLIP	0.928 \pm 0.040	5.011 \pm 0.111	10.428 \pm 0.166	5.218 \pm 0.060
	1,000	Random	1.000 \pm 0.000	5.000 \pm 0.000	10.000 \pm 0.000	5.187 \pm 0.000
		BioViL-T	1.202 \pm 0.047	4.737 \pm 0.111	8.141 \pm 0.146	4.019 \pm 0.067
		BiomedCLIP	0.914 \pm 0.043	3.389 \pm 0.094	5.885 \pm 0.129	3.013 \pm 0.059
		BioViL-T	0.153 \pm 0.018	0.697 \pm 0.042	1.311 \pm 0.061	0.726 \pm 0.026
	10,000	BiomedCLIP	0.124 \pm 0.016	0.555 \pm 0.040	0.983 \pm 0.055	0.555 \pm 0.024
		BioViL-T	0.048 \pm 0.013	0.243 \pm 0.028	0.486 \pm 0.040	0.305 \pm 0.017
	29,296	BioViL-T	0.048 \pm 0.013	0.243 \pm 0.028	0.486 \pm 0.040	0.305 \pm 0.017
		BiomedCLIP	0.044 \pm 0.013	0.201 \pm 0.026	0.402 \pm 0.037	0.237 \pm 0.016

results are summarized in Fig. 2 and Table 1, and the hard-negative results are shown in Fig. 3 and Table 2.

Retrieval weakened steadily as the candidate pool grew, but the signal did not vanish. On MIMIC-CXR, BioViL-T Recall@1 declined from 15.440% \pm 0.141 at $N = 100$ to 3.320% \pm 0.065 at $N = 1,000$, 0.496% \pm 0.027 at $N = 10,000$, and 0.150% \pm 0.019 at the full test-set size of 43,793 candidates (Table 1). On the external CheXpert Plus test set, the same model declined from 7.281% \pm 0.114 to 1.202% \pm 0.047, 0.153% \pm 0.018, and 0.048% \pm 0.013 across the same progression of candidate-pool sizes, with the full pool comprising 29,296 candidates. BiomedCLIP followed the same monotonic pattern on both datasets, indicating that the effect was not limited to a single model family. Thus, retrieval became progressively harder as the search space expanded, but the rank ordering of the models remained stable and the strongest medically adapted models continued to separate clearly from the weaker baselines. Mean reciprocal rank also decayed more gradually than Recall@1, showing that when the correct report was no longer ranked first, it often still remained near the top of the candidate list rather than disappearing into the tail of the ranking.

Relative to chance, the residual signal remained substantial. At $N = 10,000$, chance Recall@1 is 0.010%, whereas BioViL-T still reached 0.496% \pm 0.027 on MIMIC-CXR and 0.153% \pm 0.018 on CheXpert Plus, corresponding to roughly 50-fold and 15-fold chance performance, respectively. Even at full test-set size, the absolute percentages remained clearly above random matching. On MIMIC-CXR, the exact chance Recall@1 is approximately 0.002%, compared with 0.150% \pm 0.019 for BioViL-T, and on CheXpert Plus the corresponding comparison is approximately 0.003% vs. 0.048% \pm 0.013. The privacy signal is therefore not confined to artificially small candidate pools. It

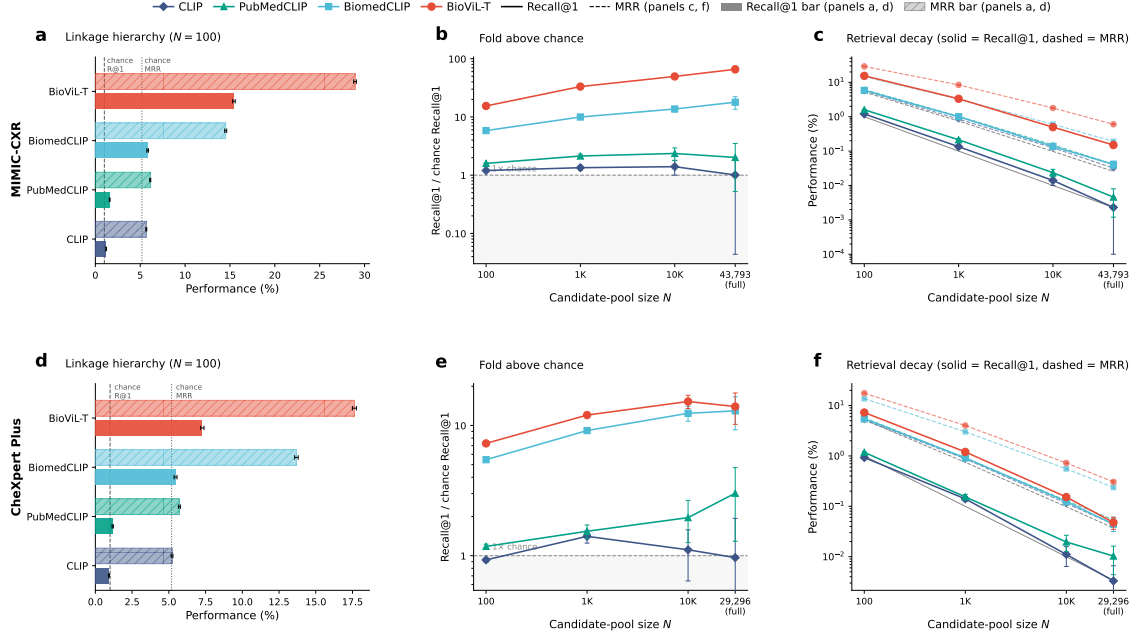


Fig. 2: Cross-modal re-linkage performance of off-the-shelf vision-language models. Each row corresponds to one evaluation cohort: MIMIC-CXR and CheXpert Plus. **a** Linkage hierarchy at $N = 100$ on MIMIC-CXR. Horizontal bars show Recall@1 (solid) and MRR (hatched) per model; vertical lines mark the corresponding chance baselines. **b** Fold-above-chance Recall@1 across candidate-pool sizes on MIMIC-CXR (log-log scale), computed as observed Recall@1 divided by exact chance Recall@1 at each N . The dashed horizontal line marks $1\times$ chance; grey shading indicates the sub-chance region. **c** Raw Recall@1 (solid) and MRR (dashed) across all candidate-pool sizes on MIMIC-CXR (log-log scale); grey lines show chance baselines. **d-f** Corresponding panels for the external CheXpert Plus cohort. Error bars in all panels represent ± 1 standard deviation across repeated random samplings of the candidate pool.

persists when retrieval is scaled to the full available database, where numerically small percentages still represent substantial enrichment over random association.

Hard negatives attenuated the signal, but did not remove it. When candidate reports at $N = 10,000$ were chosen to match the query pathology profile rather than being sampled at random, BioViL-T Recall@1 on MIMIC-CXR decreased from $0.496\% \pm 0.027$ to $0.343\% \pm 0.026$, and BiomedCLIP decreased from $0.137\% \pm 0.015$ to $0.113\% \pm 0.015$ (Table 2). On CheXpert Plus, BioViL-T decreased from $0.153\% \pm 0.018$ to $0.088\% \pm 0.017$, whereas BiomedCLIP decreased from $0.124\% \pm 0.016$ to $0.105\% \pm 0.018$. Expressed as relative reduction, the hard-negative protocol lowered Recall@1 by 30.7% for BioViL-T and 17.4% for BiomedCLIP on MIMIC-CXR, and by 42.4% and 15.2%, respectively, on CheXpert Plus (Fig. 3). What remained after pathology matching was still well above chance for the strongest models: on MIMIC-CXR, BioViL-T retained roughly 34-fold chance Recall@1 under hard negatives and BiomedCLIP remained at approximately 11-fold chance, whereas on CheXpert Plus the corresponding residual enrichments were approximately 9-fold and 10-fold chance. By contrast, PubMedCLIP and CLIP stayed only marginally above chance under the same protocol. Broad pathology similarity therefore contributed to retrieval, but did not fully account for it. The strongest clinically adapted models preserved additional image-report correspondence beyond coarse label matching alone, indicating that the shared embedding space retains finer-grained instance-level structure even under clinically constrained distractors.

Table 2: Cross-modal retrieval performance under pathology-matched hard negatives (setting B) on the MIMIC-CXR and CheXpert Plus test sets. For each query chest radiograph, the true paired report is retrieved from a candidate pool of size $N = 10,000$, where negative reports are selected to match the query 14-label pathology vector whenever possible and otherwise filled in ascending Hamming distance. Performance is evaluated using Recall@1, Recall@5, Recall@10, and mean reciprocal rank (MRR). Values are reported in percent as mean \pm standard deviation (SD) with corresponding 95% confidence intervals (CIs).

N	Model	Statistic	Recall@1	Recall@5	Recall@10	MRR	
MIMIC-CXR							
10,000	BioViL-T	Mean \pm SD	0.343 \pm 0.026	1.416 \pm 0.054	2.501 \pm 0.073	1.311 \pm 0.033	
		95% CI	[0.294, 0.396]	[1.311, 1.526]	[2.364, 2.635]	[1.248, 1.379]	
	BiomedCLIP	Mean \pm SD	0.113 \pm 0.015	0.466 \pm 0.033	0.839 \pm 0.045	0.489 \pm 0.020	
		95% CI	[0.085, 0.145]	[0.402, 0.531]	[0.749, 0.924]	[0.450, 0.530]	
	PubMedCLIP	Mean \pm SD	0.013 \pm 0.004	0.097 \pm 0.014	0.177 \pm 0.019	0.130 \pm 0.007	
		95% CI	[0.005, 0.021]	[0.070, 0.125]	[0.142, 0.217]	[0.117, 0.145]	
	CLIP	Mean \pm SD	0.012 \pm 0.004	0.086 \pm 0.013	0.155 \pm 0.017	0.116 \pm 0.006	
		95% CI	[0.004, 0.021]	[0.062, 0.112]	[0.123, 0.191]	[0.104, 0.129]	
	Random	Mean \pm SD	0.010 \pm 0.000	0.050 \pm 0.000	0.100 \pm 0.000	0.098 \pm 0.000	
		95% CI	[0.010, 0.010]	[0.050, 0.050]	[0.100, 0.100]	[0.098, 0.098]	
	CheXpert Plus						
	10,000	BioViL-T	Mean \pm SD	0.088 \pm 0.017	0.434 \pm 0.036	0.796 \pm 0.050	0.489 \pm 0.021
95% CI			[0.058, 0.125]	[0.366, 0.512]	[0.699, 0.901]	[0.451, 0.534]	
BiomedCLIP		Mean \pm SD	0.105 \pm 0.018	0.379 \pm 0.035	0.711 \pm 0.050	0.422 \pm 0.022	
		95% CI	[0.071, 0.142]	[0.311, 0.450]	[0.618, 0.806]	[0.381, 0.466]	
PubMedCLIP		Mean \pm SD	0.012 \pm 0.006	0.076 \pm 0.016	0.155 \pm 0.023	0.122 \pm 0.009	
		95% CI	[0.001, 0.026]	[0.046, 0.108]	[0.111, 0.199]	[0.105, 0.140]	
CLIP		Mean \pm SD	0.011 \pm 0.006	0.087 \pm 0.016	0.146 \pm 0.021	0.118 \pm 0.008	
		95% CI	[0.001, 0.024]	[0.055, 0.119]	[0.106, 0.189]	[0.102, 0.134]	
Random		Mean \pm SD	0.010 \pm 0.000	0.050 \pm 0.000	0.100 \pm 0.000	0.098 \pm 0.000	
		95% CI	[0.010, 0.010]	[0.050, 0.050]	[0.100, 0.100]	[0.098, 0.098]	

Head-only differential privacy finetuning reduces linkage

Targeting the shared alignment layer proved sufficient to reduce linkage. The image and text encoders were kept frozen, and only the projection heads defining the retrieval space were finetuned using differentially private optimization. On MIMIC-CXR, this intervention lowered Recall@1 at every operating point examined (Fig. 4; Table 3). The effect was already visible at small candidate pools, but became clearest at the operating points most relevant to large-scale linkage risk: BioViL-T Recall@1 fell from $0.496\% \pm 0.027$ to $0.190\% \pm 0.015$ at $N = 10,000$, from $0.150\% \pm 0.019$ to $0.039\% \pm 0.010$ at the full test-set size, and from $0.343\% \pm 0.026$ to $0.158\% \pm 0.016$ under hard negatives. MRR moved in the same direction, showing that DP finetuning shifted the ranking distribution downward rather than affecting only the top-ranked prediction.

The magnitude of this reduction was substantial. Relative to the off-the-shelf model, DP head finetuning reduced Recall@1 on MIMIC-CXR by 61.8% at $N = 10,000$, by 74.1% at full test-set size, and by 54.1% under hard negatives. The same heads, trained only on MIMIC-CXR, also reduced linkage on the external CheXpert Plus cohort without retraining, lowering Recall@1 from $0.153\% \pm 0.018$ to $0.091\% \pm 0.014$ at $N = 10,000$, from $0.048\% \pm 0.013$ to $0.034\% \pm 0.011$ at full scale, and from $0.088\% \pm 0.017$ to $0.059\% \pm 0.014$ under hard negatives. Expressed relative to chance, DP also compressed the residual enrichment above random under both the random-candidate and hard-negative settings (Fig. 4). The effect was therefore directionally consistent under external transfer, although smaller than on the in-domain cohort.

A non-private comparator clarified that not every perturbation of the alignment space is privacy-protective. Entropy-regularized head finetuning did not attenuate linkage and instead increased it across both datasets and retrieval settings. On MIMIC-CXR, for example, Recall@1

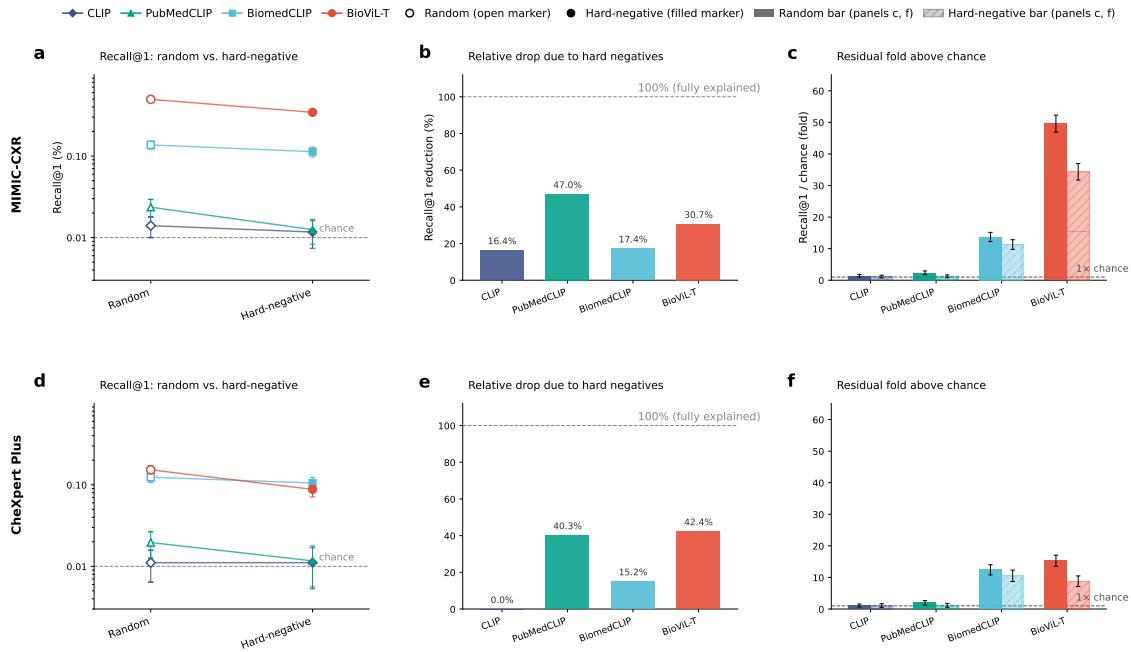


Fig. 3: Cross-modal retrieval under pathology-matched hard negatives at $N = 10,000$. Each row corresponds to one evaluation cohort: MIMIC-CXR and CheXpert Plus. **a** Recall@1 before and after replacing random distractors with pathology-matched hard negatives on MIMIC-CXR. Each model is shown as a slope from the random-candidate protocol (open marker) to the hard-negative protocol (filled marker); the dashed horizontal line marks chance Recall@1 at $N = 10,000$. **b** Percentage reduction in Recall@1 induced by hard negatives per model on MIMIC-CXR. Bars reaching 100% would indicate that pathology similarity fully accounts for retrieval; the modest observed values show that residual instance-level binding persists beyond label matching alone. **c** Fold-above-chance Recall@1 under both protocols on MIMIC-CXR. Solid bars show the random-candidate protocol and hatched bars show the hard-negative protocol; the horizontal dashed line marks $1\times$ chance. The strongest medically adapted models remain well above chance even after the hard-negative drop. **d-f** Corresponding panels for the external CheXpert Plus cohort. Error bars, where shown, represent ± 1 standard deviation.

increased from $0.496\% \pm 0.027$ to $0.924\% \pm 0.036$ at $N = 10,000$ and from $0.343\% \pm 0.026$ to $0.682\% \pm 0.036$ under hard negatives. On CheXpert Plus, the same comparator increased Recall@1 from $0.153\% \pm 0.018$ to $0.402\% \pm 0.031$ at $N = 10,000$ and from $0.088\% \pm 0.017$ to $0.272\% \pm 0.030$ under hard negatives. The amplification was also evident in the chance-normalized view, especially on the external cohort. The mitigation result is therefore not explained by merely changing the projection heads. What matters is changing them in a way that weakens image-report coupling rather than sharpening it.

DP mitigation preserves image-side diagnostic utility

The decisive question for any privacy intervention is whether it reduces linkage without erasing clinically useful image information. To assess that tradeoff directly, image-side utility was evaluated separately from retrieval by training linear probes on fixed BioViL-T image embeddings for the standard 14-label chest radiograph task. Figure 5 and Table 4 summarize the main results, and the full per-label values are provided in Supplementary Table 3.

Table 3: Mitigation of cross-modal linkage risk in BioViL-T under head-only finetuning. Retrieval performance is shown after projection-head finetuning with either differentially private (DP) optimization or entropy regularization, while the image and text backbones remain frozen. Random denotes the random-candidate protocol and Hard-neg denotes the pathology-matched hard-negative protocol. For CheXpert Plus, the BioViL-T projector heads trained on MIMIC-CXR were applied directly without additional mitigation training. The image and text backbones remained frozen throughout. Performance is evaluated using Recall@1, Recall@5, Recall@10, and mean reciprocal rank (MRR). Values are reported in percent as mean \pm standard deviation (SD) with corresponding 95% confidence intervals (CIs).

Variant	Setting	N	Statistic	Recall@1	Recall@5	Recall@10	MRR
MIMIC-CXR							
DP	Random	100	Mean \pm SD	9.416 \pm 0.106	29.398 \pm 0.191	43.859 \pm 0.220	20.501 \pm 0.123
			95% CI	[9.211, 9.635]	[29.020, 29.787]	[43.442, 44.311]	[20.272, 20.755]
		1,000	Mean \pm SD	1.547 \pm 0.043	6.153 \pm 0.102	10.413 \pm 0.136	4.937 \pm 0.061
			95% CI	[1.467, 1.633]	[5.957, 6.364]	[10.149, 10.693]	[4.822, 5.057]
	10,000	Mean \pm SD	0.190 \pm 0.015	0.874 \pm 0.039	1.662 \pm 0.055	0.895 \pm 0.023	
		95% CI	[0.161, 0.222]	[0.799, 0.952]	[1.559, 1.775]	[0.851, 0.941]	
	43,786	Mean \pm SD	0.039 \pm 0.009	0.216 \pm 0.022	0.418 \pm 0.030	0.264 \pm 0.012	
		95% CI	[0.021, 0.059]	[0.174, 0.260]	[0.361, 0.475]	[0.242, 0.290]	
Hard-neg	10,000	Mean \pm SD	0.158 \pm 0.016	0.718 \pm 0.038	1.416 \pm 0.055	0.785 \pm 0.022	
		95% CI	[0.125, 0.190]	[0.641, 0.792]	[1.312, 1.524]	[0.741, 0.830]	
Entropy	Random	100	Mean \pm SD	22.137 \pm 0.158	51.312 \pm 0.222	65.419 \pm 0.214	36.224 \pm 0.162
			95% CI	[21.823, 22.452]	[50.882, 51.739]	[65.001, 65.843]	[35.898, 36.548]
		1,000	Mean \pm SD	5.379 \pm 0.082	17.026 \pm 0.165	25.617 \pm 0.201	12.118 \pm 0.104
			95% CI	[5.232, 5.553]	[16.705, 17.362]	[25.213, 26.017]	[11.923, 12.326]
	10,000	Mean \pm SD	0.924 \pm 0.036	3.516 \pm 0.078	5.968 \pm 0.102	2.886 \pm 0.049	
		95% CI	[0.855, 0.998]	[3.372, 3.675]	[5.780, 6.180]	[2.800, 2.990]	
	43,793	Mean \pm SD	0.291 \pm 0.026	1.082 \pm 0.049	1.914 \pm 0.065	1.027 \pm 0.030	
		95% CI	[0.240, 0.343]	[0.989, 1.183]	[1.790, 2.042]	[0.971, 1.087]	
Hard-neg	10,000	Mean \pm SD	0.682 \pm 0.036	2.670 \pm 0.073	4.727 \pm 0.097	2.313 \pm 0.044	
		95% CI	[0.614, 0.753]	[2.532, 2.817]	[4.543, 4.912]	[2.231, 2.403]	
CheXpert Plus							
DP	Random	100	Mean \pm SD	4.562 \pm 0.091	17.304 \pm 0.185	30.019 \pm 0.232	13.140 \pm 0.111
			95% CI	[4.382, 4.744]	[16.961, 17.681]	[29.550, 30.476]	[12.926, 13.369]
		1,000	Mean \pm SD	0.648 \pm 0.034	2.772 \pm 0.085	4.943 \pm 0.116	2.596 \pm 0.050
			95% CI	[0.580, 0.714]	[2.605, 2.931]	[4.726, 5.166]	[2.499, 2.694]
	10,000	Mean \pm SD	0.090 \pm 0.014	0.334 \pm 0.029	0.645 \pm 0.043	0.428 \pm 0.019	
		95% CI	[0.064, 0.120]	[0.278, 0.390]	[0.559, 0.729]	[0.391, 0.467]	
	29,296	Mean \pm SD	0.034 \pm 0.011	0.143 \pm 0.022	0.245 \pm 0.028	0.179 \pm 0.013	
		95% CI	[0.014, 0.055]	[0.102, 0.188]	[0.191, 0.297]	[0.157, 0.207]	
Hard-neg	10,000	Mean \pm SD	0.059 \pm 0.014	0.244 \pm 0.027	0.471 \pm 0.037	0.333 \pm 0.017	
		95% CI	[0.032, 0.089]	[0.192, 0.296]	[0.401, 0.546]	[0.301, 0.367]	
Entropy	Random	100	Mean \pm SD	13.830 \pm 0.153	39.344 \pm 0.263	55.276 \pm 0.274	26.847 \pm 0.170
			95% CI	[13.533, 14.100]	[38.841, 39.837]	[54.775, 55.812]	[26.515, 27.162]
		1,000	Mean \pm SD	2.627 \pm 0.072	9.579 \pm 0.146	15.624 \pm 0.195	7.268 \pm 0.093
			95% CI	[2.491, 2.774]	[9.291, 9.863]	[15.253, 16.001]	[7.088, 7.448]
	10,000	Mean \pm SD	0.402 \pm 0.031	1.588 \pm 0.069	2.795 \pm 0.091	1.483 \pm 0.043	
		95% CI	[0.340, 0.465]	[1.458, 1.728]	[2.623, 2.975]	[1.401, 1.574]	
	29,296	Mean \pm SD	0.158 \pm 0.023	0.664 \pm 0.049	1.208 \pm 0.065	0.666 \pm 0.029	
		95% CI	[0.109, 0.205]	[0.570, 0.768]	[1.075, 1.341]	[0.609, 0.725]	
Hard-neg	10,000	Mean \pm SD	0.272 \pm 0.030	1.079 \pm 0.061	2.045 \pm 0.084	1.088 \pm 0.037	
		95% CI	[0.214, 0.334]	[0.960, 1.201]	[1.891, 2.211]	[1.016, 1.163]	

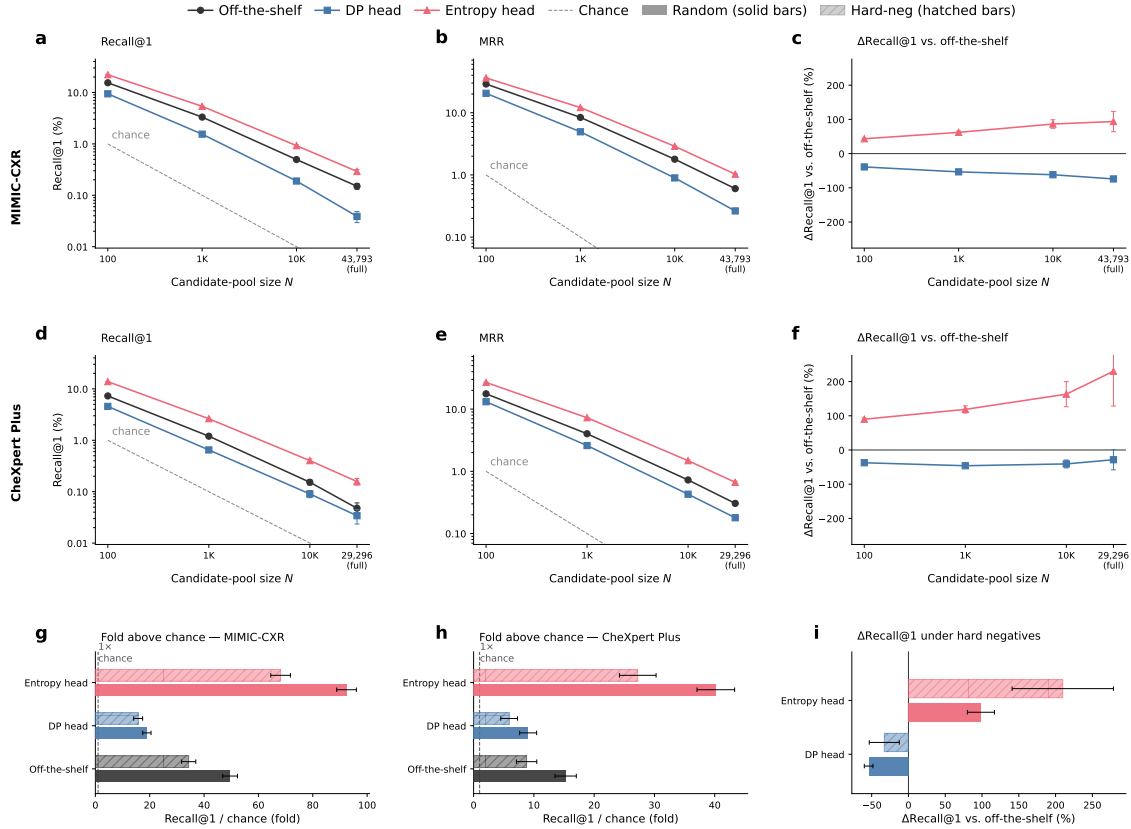


Fig. 4: Mitigation of cross-modal linkage through head-only finetuning of BioViL-T. Each row in the upper two sections corresponds to one evaluation cohort: MIMIC-CXR and CheXpert Plus. **a** Recall@1 across candidate-pool sizes on MIMIC-CXR under the random-candidate protocol, comparing off-the-shelf, DP head finetuning, and entropy-regularized head finetuning. The grey dashed line marks chance Recall@1 at each N . **b** MRR across candidate-pool sizes on MIMIC-CXR under the same three variants. **c** Percentage change in Recall@1 relative to the off-the-shelf model across candidate-pool sizes on MIMIC-CXR. Negative values indicate reduced linkage; positive values indicate amplified linkage. The horizontal line marks zero change. **d–f** Corresponding panels for the external CheXpert Plus cohort, using the same heads trained on MIMIC-CXR without retraining. **g** Fold-above-chance Recall@1 at $N = 10,000$ on MIMIC-CXR under hard negatives (hatched) and the random-candidate protocol (solid) for each variant; the vertical dashed line marks $1\times$ chance. **h** Corresponding panel for CheXpert Plus. **i** Percentage change in Recall@1 relative to off-the-shelf under hard negatives at $N = 10,000$, for both cohorts (MIMIC-CXR solid, CheXpert Plus hatched). Error bars represent ± 1 standard deviation.

Table 4: Image-side diagnostic utility of BioViL-T embeddings before and after DP head finetuning. Utility was assessed on the MIMIC-CXR test set using image-only linear probing on the standard 14-label chest radiograph task. Macro AUROC was the primary utility endpoint. Values are reported in percent as mean \pm standard deviation followed by the corresponding 95% confidence interval, Δ denotes DP minus off-the-shelf performance in percentage points, and p-values were computed from 1,000 paired bootstrap replicates.

Metric	Off-the-shelf	DP head finetuning	Δ	P-value
Summary metrics				
Macro AUROC	79.63 \pm 0.15 [79.32, 79.90]	79.43 \pm 0.15 [79.13, 79.72]	-0.20	0.006
Macro accuracy	89.39 \pm 0.04 [89.31, 89.48]	89.37 \pm 0.04 [89.29, 89.46]	-0.02	0.294
Macro sensitivity	19.44 \pm 0.09 [19.25, 19.62]	19.75 \pm 0.10 [19.56, 19.95]	+0.31	0.002
Macro specificity	96.88 \pm 0.03 [96.83, 96.93]	96.79 \pm 0.03 [96.74, 96.84]	-0.08	0.002
Representative per-label AUROC				
Atelectasis	80.03 \pm 0.24 [79.56, 80.49]	79.88 \pm 0.24 [79.41, 80.34]	-0.15	0.078
Cardiomegaly	80.53 \pm 0.23 [80.06, 80.98]	80.17 \pm 0.24 [79.69, 80.64]	-0.36	0.002
Edema	88.89 \pm 0.20 [88.50, 89.27]	88.71 \pm 0.20 [88.33, 89.11]	-0.18	0.006
Lung opacity	75.77 \pm 0.28 [75.24, 76.32]	75.81 \pm 0.27 [75.27, 76.33]	+0.03	0.729
No finding	84.25 \pm 0.19 [83.87, 84.64]	84.23 \pm 0.19 [83.88, 84.62]	-0.01	0.745
Pleural effusion	88.81 \pm 0.17 [88.48, 89.16]	88.54 \pm 0.18 [88.19, 88.88]	-0.28	0.002
Pneumothorax	80.59 \pm 0.48 [79.59, 81.52]	80.86 \pm 0.49 [79.84, 81.80]	+0.26	0.340
Support devices	87.05 \pm 0.18 [86.69, 87.40]	86.98 \pm 0.18 [86.61, 87.33]	-0.07	0.240

The central pattern was strongly asymmetric. The same DP intervention that reduced Recall@1 by 61.8% at $N = 10,000$ preserved 99.7% of the off-the-shelf macro AUROC (Fig. 5). In absolute terms, macro AUROC changed only from 79.63% \pm 0.15 to 79.43% \pm 0.15, a decrease of 0.20 percentage points, whereas macro accuracy was essentially unchanged at 89.39% \pm 0.04 vs. 89.37% \pm 0.04 (Table 4). Paired bootstrap analysis showed that the AUROC decrease was small but consistent, while accuracy remained centered near zero change (Fig. 5). By contrast, sensitivity increased slightly from 19.44% \pm 0.09 to 19.75% \pm 0.10 and specificity decreased slightly from 96.88% \pm 0.03 to 96.79% \pm 0.03, indicating a modest redistribution of the operating point rather than broad loss of predictive structure.

The per-label analysis supports the same interpretation. AUROC changes were small and mixed rather than uniformly negative. Some labels showed modest decreases, including enlarged cardio-mediastinum, cardiomegaly, edema, and pleural effusion, whereas others changed little or moved slightly upward, such as pneumothorax and fracture (Fig. 5; Supplementary Table 3). The largest metric shifts were concentrated in sensitivity and specificity rather than in AUROC itself (Fig. 5), again suggesting mild threshold-level reshaping more than destruction of the underlying image representation. Taken together with the retrieval results above, the findings show an important tradeoff of the study: head-only DP finetuning weakened privacy-relevant cross-modal binding far more than it weakened downstream image-side diagnostic signal.

Discussion

This study shows that the shared image-text embeddings learned by clinical VLMs preserve recoverable instance-level image-report structure, which constitutes a cross-modal privacy risk in deployments where that pairing is meant to remain separate. Across two public chest radiograph cohorts, off-the-shelf models were able to re-link a held-out radiograph to its paired report, and the strength of that linkage increased systematically with domain specialization. The radiology-specific BioViL-T [6] model consistently showed the strongest signal, the effect remained above chance at database scale and under pathology-matched hard negatives, and head-only differentially private finetuning of the shared alignment layer substantially reduced that signal while largely preserving

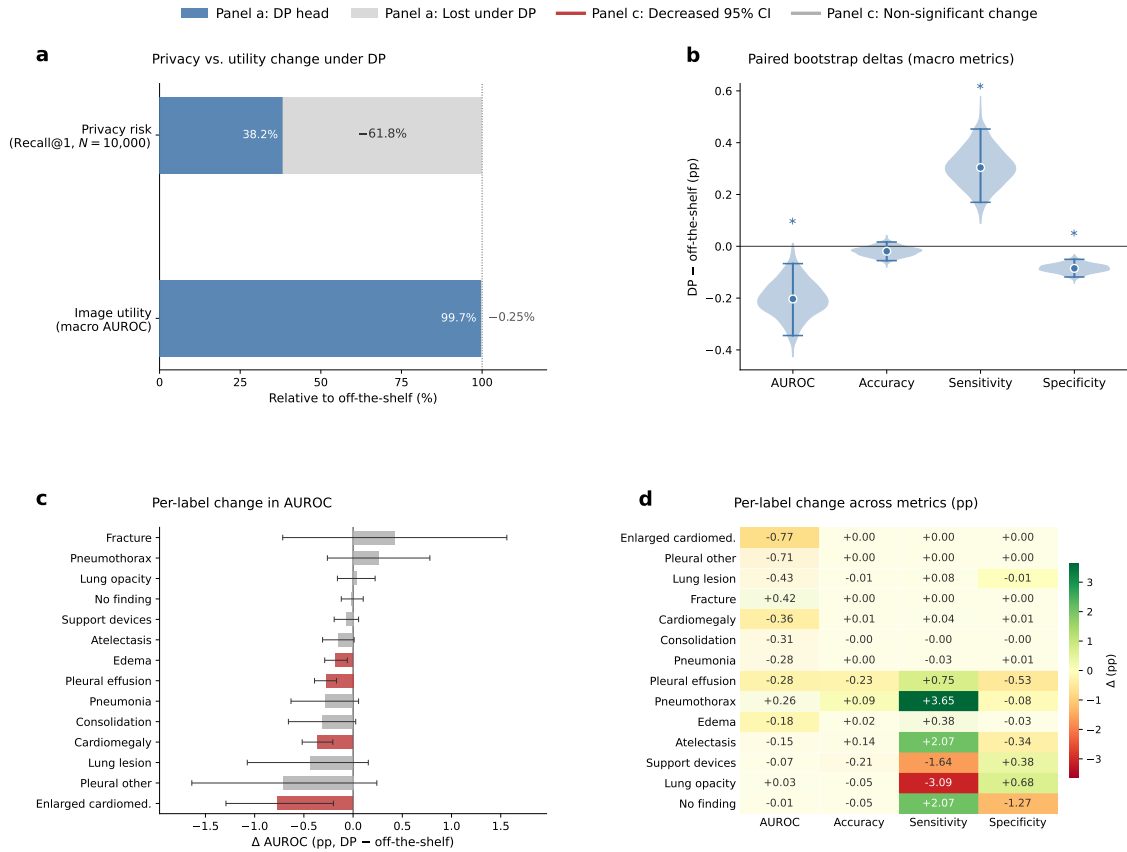


Fig. 5: Image-side diagnostic utility after DP mitigation. All panels compare off-the-shelf BioViL-T and DP-mitigated BioViL-T image embeddings on the MIMIC-CXR 14-label chest radiograph task. DP statistics were computed from 1,000 paired bootstrap replicates. **a** Asymmetry of the privacy-utility tradeoff. Bars show Recall@1 at $N = 10,000$ (top) and macro AUROC (bottom) for the DP-mitigated model, normalized to the off-the-shelf value (100%). Blue segments show what remains under DP, grey segments show what was lost; the relative reduction is annotated in each segment. **b** Paired bootstrap distributions of the DP-minus-off-the-shelf delta for the four macro utility metrics. Violins show the distribution over 1,000 replicates; filled circles mark the median and vertical bars span the 95% bootstrap CI. Metrics whose CI excludes zero are marked with *. **c** Per-label change in AUROC. Bars are color-coded by the direction and statistical significance of the change: green if the 95% CI is strictly positive, red if strictly negative, grey otherwise. **d** Per-label delta across all four utility metrics. Rows are 14 pathology labels sorted by $|\Delta$ AUROC|; columns are AUROC, accuracy, sensitivity, and specificity. Cells are colored by difference in percentage points; non-significant cells (95% CI includes zero) are whitened.

image-side diagnostic utility. In this sense, the study identifies multimodal alignment itself as the central object of both capability and risk in clinical VLMs [15,4,5,6].

The main conceptual point is that this privacy problem is not well described by standard de-identification alone and is not identical to the image-only privacy settings more commonly discussed in medical AI [9,10,11,14]. What becomes vulnerable in a clinical VLM is not only an image representation or a text representation in isolation, but the learned correspondence between them. In our results, the strongest clinically adapted models could recover paired reports at rates far above random even though explicit identifiers were absent, and that effect transferred externally from MIMIC-CXR to CheXpert Plus. This matters because radiology reports are much richer than categorical labels, often containing narrative findings, technical qualifiers, comparisons, and contextual detail that substantially increase the sensitivity of a successful re-linkage event [7,8].

The ordering of models also provides an important clue about mechanism. Risk rose from general-domain CLIP to PubMedCLIP and BiomedCLIP, and was highest in BioViL-T, the model most closely adapted to chest radiograph reporting [19,26,24,6]. That pattern is difficult to reconcile with a purely generic image-matching effect. Instead, it suggests that clinical specialization sharpens image-report binding in the shared embedding space. The external results support the same interpretation. Absolute linkage weakened outside the in-domain cohort, but the rank ordering persisted, implying that the learned binding is not a narrow artefact of a single dataset split. More broadly, the results suggest that the same specialization that makes a multimodal model clinically useful can also intensify its capacity to reconnect paired patient data.

A second major finding is that the linkage signal survives settings that are much more stringent than a small retrieval pool. Absolute Recall@1 declined as the candidate pool expanded, but fold-enrichment over chance remained large at $N = 10,000$ and at full-database scale. Likewise, pathology-matched hard negatives reduced retrieval, but did not eliminate it. This is important because coarse disease similarity is the most obvious alternative explanation for retrieval success. Our hard-negative results show that broad pathology overlap explains part of the signal, but not all of it. The strongest medically adapted models retained substantial residual enrichment above chance even when distractor reports were forced to match the same 14-label pathology profile. Taken together, these findings argue that the shared embedding space retains finer-grained instance-level structure beyond broad diagnostic category matching [18,16]. In practical terms, the privacy risk is therefore not confined to artificial toy settings with small candidate pools or easy negatives.

The mitigation results further clarify where that risk lives. Freezing the image and text encoders and updating only the projection heads was sufficient to reduce linkage across candidate-pool sizes, reduce mean reciprocal rank in parallel with Recall@1, and transfer directionally to an external cohort without retraining. This points to the final shared alignment layer as a particularly important intervention point. The relevant privacy signal appears to be mediated less by wholesale destruction of the unimodal backbones than by how those backbones are brought together in the retrieval space [6,19]. At the same time, the results also show that not every intervention on the projection heads is privacy-protective. The entropy-regularized comparator increased linkage rather than decreasing it, often quite substantially. Thus, the mitigation effect cannot be explained by perturbing the heads in a generic way. What matters is whether the update weakens exact pairwise coupling or instead sharpens it.

The privacy-utility tradeoff was notably asymmetric. The DP intervention reduced Recall@1 by 61.8% at $N = 10,000$ on MIMIC-CXR, while preserving 99.7% of the off-the-shelf macro AUROC in the image-only utility analysis. Macro accuracy remained essentially unchanged, and most of the observed utility differences were concentrated in sensitivity and specificity rather than in AUROC itself. The per-label results showed small and mixed AUROC changes rather than uniform collapse, which is more consistent with mild reshaping of the representation and operating point than

with wholesale destruction of clinically useful image information. This asymmetry is encouraging because it suggests that privacy-relevant cross-modal binding can be weakened more strongly than downstream image-side signal. At the same time, the AUROC decrease was not literally zero, and some threshold-dependent metrics moved non-trivially. The tradeoff is therefore favorable, but not free.

These findings have direct implications for how clinical multimodal checkpoints should be evaluated and released. Because public paired datasets publish the image-report correspondence by design, the risk we measured is operational not within those datasets but in deployments where that correspondence is deliberately withheld, such as image-only data sharing, access-controlled reporting, institutional data enclaves, and model evaluation pipelines; the public cohorts served as ground-truth benchmarks that make the underlying recoverability measurable. Current reporting of medical VLMs focuses mainly on downstream task performance, zero-shot transfer, or report generation quality [1,2], although recent clinical LLM evidence shows that safety can diverge from average accuracy and scale [28]. Our results suggest that this is incomplete, consistent with recent radiology LLM work showing that reliability can depend strongly on framing and evaluation context [29]. Shared embeddings should also be stress-tested for cross-modal re-linkage risk, including database-scale retrieval, chance-normalized analyses, and clinically constrained hard negatives. That recommendation is especially relevant for public checkpoints that may later be downloaded, reused, or finetuned on de-identified hospital data [1,17]. In that setting, privacy cannot be treated only as a preprocessing issue at the dataset level; it also becomes a property of the learned multimodal geometry.

The study also suggests a practical mitigation direction. Full-model private retraining of large multimodal encoders is often computationally unstable or prohibitively expensive. By contrast, projector-only DP finetuning is comparatively lightweight, leaves the backbones intact, and can be applied after pretraining. This makes it a plausible candidate for post hoc risk reduction when a model already exists and the question is how to deploy or adapt it more safely [12,13]. However, the formal privacy guarantee in our study applies to the projector-head training procedure itself, not to the original pretraining of the frozen backbones or to all possible downstream uses of the released checkpoint. The mitigation should therefore be viewed as a targeted reduction of one specific linkage mechanism rather than as a complete solution to multimodal privacy.

Several limitations should be considered. First, the study is limited to chest radiography and to public cohorts from two institutions. The extent to which the same magnitude of risk appears in other imaging modalities, report styles, or multilingual reporting settings remains unknown. Second, the threat model is retrieval-based and retrospective, and it was instantiated on public cohorts in which the image-report pairing is available by design. These cohorts were chosen deliberately as ground-truth benchmarks, since known pairing is what makes recoverability measurable, but they are a proxy for the deployment settings of real interest, in which reports are withheld from the image side. The study therefore does not directly observe an end-to-end attack in such a deployment, and it does not exhaust all possible adversarial settings, external corpora, or report distributions. Third, mitigation was studied only for BioViL-T, because it exhibited the strongest off-the-shelf linkage. Although this was the most relevant target, other architectures may respond differently to projector-only private training. Fourth, our hard-negative construction relied on a 14-label pathology space. This is a strong control for broad disease overlap, but it is still a relatively coarse clinical summary and cannot fully represent all report-level nuance. Fifth, image-side utility was evaluated through linear probing rather than through a broader set of downstream clinical tasks. This isolates representation quality cleanly, but it does not capture every clinically relevant use case. Finally, if the current utility pipeline is not rerun with strict validation-based checkpoint selection before final submission, the reported utility values should be interpreted as interim and potentially optimistic.

Despite these limitations, the central message is clear. In clinical VLMs, multimodal alignment is both a strength and a liability. It enables powerful cross-modal retrieval and clinically useful representations, but it can also preserve enough pairwise structure to reconnect de-identified images to their original reports. Our results show that this risk is measurable in off-the-shelf models, amplified by domain specialization, and only partially explained by coarse pathology similarity. They also show that targeted head-only DP finetuning can materially weaken that risk without materially erasing image-side diagnostic value. Responsible evaluation of clinical multimodal models should therefore ask not only what shared embeddings can align, but also what they may unintentionally reconnect.

Materials and Methods

Ethics statement

All methods were performed in accordance with relevant guidelines and regulations. This study used solely publicly available chest radiograph datasets and, therefore, institutional review board approval and individual informed consent were not required.

Study design

The study was designed to quantify and mitigate cross-modal linkage risk in clinical VLMs. The central question was whether a held-out chest radiograph could be re-linked to its original radiology report by ranking candidate reports in a shared image-text embedding space. Because MIMIC-CXR and CheXpert Plus publish the image-report pairing by design, we used them as ground-truth benchmarks to audit this recoverability rather than as the privacy scenario itself; the operational concern targeted here is deployments in which radiographs and reports are deliberately kept separate after acquisition, where a shared embedding space could weaken that intended separation. We formalized this risk as an image-to-report retrieval task and evaluated four publicly available VLMs spanning increasing degrees of domain specialization, namely CLIP [19], PubMedCLIP [26], BiomedCLIP [24], and BioViL-T [6]. The primary evaluation was performed on a held-out MIMIC-CXR test set [3], and external generalization was assessed on a held-out CheXpert Plus test set [21,20]. Retrieval was studied under two complementary protocols. The first was a random-candidate protocol in which the true paired report was ranked against candidate pools of increasing size, from small pools to the full test set. The second was a pathology-matched hard-negative protocol in which distractor reports were selected to be clinically similar to the query case in order to reduce the extent to which retrieval could succeed through broad disease similarity alone.

The analysis proceeded in three stages. First, we measured off-the-shelf cross-modal linkage across model families, candidate-pool sizes, and datasets. Second, we tested whether linkage could be reduced by modifying only the final shared alignment space while keeping the image and text backbones frozen, using head-only differentially private finetuning [30] as the main mitigation and entropy-regularized [22] head finetuning as a non-private comparator. Third, we quantified the privacy-utility tradeoff by testing whether the mitigated image embeddings retained clinically useful information in an image-only linear-probe setting on the standard 14-label chest radiograph abnormality task [21].

Data sources and cohort construction

This study used two large-scale public chest radiograph resources including a total of $n=406,241$ paired image-report examples from 126,804 patients. MIMIC-CXR served as the primary development and evaluation cohort, and CheXpert Plus served as the external evaluation cohort. Table 5

Table 5: Characteristics of the datasets utilized in this study. Summary of patient cohorts, AP/PA-filtered radiograph counts, demographics, label sets, and projection distributions for the two chest-radiograph datasets used in this work, namely MIMIC-CXR and CheXpert Plus. Reported values include the number of patients and radiographs after restriction to frontal anteroposterior (AP) and posteroanterior (PA) images, split into training, validation, and test sets, together with age summaries and sex ratios where available. The labels listed correspond to the 14-label abnormality space used for hard-negative construction and image-side utility evaluation. The row “Final held-out retrieval cohort” reports the paired test cohort actually analyzed in the manuscript. N/A = not available from the supplied filtered source file.

Characteristic	MIMIC-CXR	CheXpert Plus
Role in study	Primary development and evaluation cohort	External evaluation cohort
Location	Boston, MA, USA	Stanford, CA, USA
Number of patients (total, n)	62,094	64,710
Number of patients (training set, n)	44,510	48,533
Number of patients (validation set, n)	5,465	6,471
Number of patients (test set, n)	12,119	9,706
Number of radiographs (total, n)	215,187	191,054
Number of radiographs (training set, n)	153,255	142,809
Number of radiographs (validation set, n)	18,139	19,534
Number of radiographs (test set, n)	43,793	28,711
Final held-out retrieval cohort	43,793	29,293
Patient age (years), median	N/A	62
Patient age (years), mean \pm SD	N/A	60.6 \pm 17.8
Patient age (years), range	N/A	(10, 89)
Patient sex (female/male/unknown, training set, %)	N/A	41.1 / 58.8 / 0.1
Patient sex (female/male/unknown, test set, %)	N/A	42.6 / 57.3 / 0.1
Projection distribution (AP, %)	58.2	84.6
Projection distribution (PA, %)	41.8	15.4
Labels used in this study	atelectasis, cardiomegaly, consolidation, edema, enlarged cardiomeastinum, fracture, lung lesion, lung opacity, no finding, pleural effusion, pleural other, pneumonia, pneumothorax, support devices	

summarizes the cohort characteristics, split structure, demographic information where available, and the label space used in this study.

MIMIC-CXR. MIMIC-CXR [3] is a large public chest radiograph dataset from Beth Israel Deaconess Medical Center in Boston, Massachusetts, USA, containing de-identified chest radiographs linked to free-text radiology reports. In the finalized cohort used in this study, MIMIC-CXR comprised 215,187 frontal radiographs from 62,094 patients. Because the available official test split too small in size, a new patient-stratified random split was created specifically for this study, with 80% of patients assigned to training and 20% to test, and 10% of the training partition reserved for validation. The final held-out MIMIC-CXR retrieval cohort analyzed in the manuscript comprised 43,793 paired image-report examples. The same split logic was preserved throughout off-the-shelf retrieval evaluation, hard-negative analysis, mitigation training, post-mitigation retrieval evaluation, and image-side utility analysis.

CheXpert Plus. CheXpert Plus [20] is an extension of the original CheXpert [21] benchmark in which the chest radiographs are supplemented with their corresponding radiology reports and associated metadata. CheXpert Plus contained 191,054 frontal image-report rows from 64,710 patients. The final external retrieval cohort analyzed in the manuscript comprised 29,293 paired image-report examples. CheXpert Plus was used exclusively for external evaluation and was not used for mitigation training.

Image preprocessing and label space

Only frontal chest radiographs in anteroposterior (AP) or posteroanterior (PA) view were used [31,32,27,33]. The same image-processing pipeline was applied across MIMIC-CXR and CheXpert Plus so that off-the-shelf retrieval, mitigation training, post-mitigation retrieval, and image-side utility evaluation were directly comparable. Images were resized to 224×224 pixels for model input [27,34,32,33]. Pixel intensities were normalized using the standard scheme of subtracting the minimum pixel value, dividing by the maximum of the shifted image, clipping to the valid range, converting to unsigned integer values in $[0, 255]$, and then applying histogram equalization [31,3]. Subject and study identifiers were retained only for split control and bookkeeping and were not provided to the models as predictive inputs [31,3].

The pathology label space consisted of the standard 14 chest radiograph labels: atelectasis, cardiomegaly, consolidation, edema, enlarged cardiomeastinum, fracture, lung lesion, lung opacity, no finding, pleural effusion, pleural other, pneumonia, pneumothorax, and support devices. These labels were encoded as binary vectors [31,32,27,33] and were used both to construct pathology-matched hard negatives and to define the downstream image-only utility task. For MIMIC-CXR, we used the labels generated with the CheXpert labeler [21] so that the label space remained aligned with CheXpert Plus. For the supervised utility analysis, only the original positive class was treated as positive. Negative, uncertain, and not-mentioned labels were grouped into the negative class, and missing labels were excluded through masking during loss computation. Dataset-level label prevalences and any additional label-processing details are reported in Supplementary Table 4.

Off-the-shelf vision-language models

We evaluated four publicly available VLMs spanning increasing levels of medical specialization: the general-domain CLIP model [19], the biomedical models PubMedCLIP [26] and BiomedCLIP [24], and the radiology-specific BioViL-T [6]. This set was chosen to cover the range from generic image-text alignment to chest-radiology-specialized multimodal alignment.

For CLIP and PubMedCLIP, image and text embeddings were extracted with the corresponding Hugging Face processor-model interfaces. BiomedCLIP embeddings were obtained through OpenCLIP with the checkpoint-specific tokenizer. For BioViL-T, image embeddings were extracted with the radiology-specific image inference interface in `health_multimodal` (<https://github.com/microsoft/hi-ml/tree/main/hi-ml-multimodal>), and text embeddings were obtained from the corresponding pretrained text encoder through its remote-code interface. In all cases, retrieval used the final shared image-text embedding space exposed by the pretrained checkpoint, with image and text embeddings ℓ_2 -normalized before similarity computation. Text inputs were truncated to the model-specific tokenization limits to avoid sequence overflow. Tokenizer settings, truncation limits, loading interfaces, and embedding dimensions are reported in Supplementary Table 5.

We considered an adversary with access to de-identified chest radiographs, or to their image embeddings, who seeks to recover the narrative report originally associated with each image while the reports are held separately, for example under independent access control or in an image-only release. Public paired cohorts were used only to instantiate and score this attack: because the true image-report pairing is known in MIMIC-CXR and CheXpert Plus, it provides the ground truth needed to measure whether the shared embedding space makes the correct report recoverable. Retrieval success on these benchmarks therefore estimates how strongly a model would enable re-linkage in a deployment where such separation is intended, and is not itself a breach of these public datasets.

Image-to-report retrieval threat model

The privacy threat model was formulated as an image-to-report retrieval task. For a query chest radiograph x_i , let r_i denote its true paired report, and let $\mathcal{R}_i = \{r_i, r_{j_1}, \dots, r_{j_{N-1}}\}$ denote the candidate pool containing the true report together with $N - 1$ distractor reports. Let z_i^{img} denote the normalized image embedding of x_i and let z_j^{text} denote the normalized text embedding of candidate report r_j . Ranking was performed by cosine similarity in the shared embedding space,

$$s(x_i, r_j) = \frac{z_i^{\text{img}} \cdot z_j^{\text{text}}}{\|z_i^{\text{img}}\|_2 \|z_j^{\text{text}}\|_2}. \quad (1)$$

Because all embeddings were ℓ_2 -normalized before retrieval, this score reduces to the dot product in the shared space. Candidate reports were sorted in descending order of $s(x_i, r_j)$, and the rank of the true paired report within the pool was recorded for each query.

The primary privacy endpoint was Recall@1, interpreted as the proportion of query images for which the true paired report was ranked first. Secondary privacy endpoints were Recall@5, Recall@10, and mean reciprocal rank (MRR). For M query images, Recall@X was defined as

$$\text{Recall@X} = \frac{1}{M} \sum_{i=1}^M \mathbf{1}[\text{rank}_i \leq X], \quad (2)$$

Moreover, MRR is defined as,

$$\text{MRR} = \frac{1}{M} \sum_{i=1}^M \frac{1}{\text{rank}_i}. \quad (3)$$

These metrics quantify how strongly a model preserves image-report correspondence in the shared embedding space. In this framework, higher retrieval performance corresponds to higher cross-modal linkage risk because it indicates that the true paired report remains easier to recover from among competing reports.

Retrieval protocols

Two retrieval protocols were used. The first protocol was the random-candidate setting, denoted Setting A in the study workflow. The second protocol was the pathology-matched hard-negative setting, denoted Setting B. Together, these two protocols were designed to distinguish simple retrieval in randomly sampled candidate pools from a stricter setting in which distractor reports were intentionally chosen to resemble the query case clinically.

Setting A: random-candidate retrieval. In the random-candidate protocol, each query chest radiograph x_i was evaluated against a candidate pool containing its true paired report together with randomly sampled alternative reports from the same held-out split. The candidate pool was therefore

$$\mathcal{R}_i^{(A)} = \{r_i\} \cup \mathcal{N}_i^{(A)}, \quad (4)$$

where r_i is the true paired report and $\mathcal{N}_i^{(A)}$ contains $N - 1$ distractor reports sampled without replacement from the same evaluation split after excluding the true pair. Candidate-pool sizes were $N = 100$, $N = 1,000$, $N = 10,000$, and the full available test-set size. For MIMIC-CXR, the full-pool condition therefore corresponded to 43,793 candidate reports, and for CheXpert Plus it corresponded to 29,296 candidate reports. To reduce dependence on a single random draw, candidate-pool construction in Setting A was repeated 20 times per query. Retrieval metrics were first averaged at the query level across these repeated candidate pools and were then aggregated across all query images to produce the reported dataset-level results.

Setting B: pathology-matched hard negatives. In the hard-negative protocol, distractor reports were selected to be clinically similar to the query case rather than sampled at random. Let $y_i \in \{0, 1\}^{14}$ denote the binary pathology label vector for query i . We first identified all reports with an identical label vector, $\mathcal{E}_i = \{r_j : y_j = y_i, j \neq i\}$, and used these exact pathology matches as the first source of candidate negatives. When the exact-match pool was insufficient, the remaining slots were filled in ascending Hamming distance,

$$d_H(y_i, y_j) = \sum_{k=1}^{14} \mathbf{1}[y_{ik} \neq y_{jk}], \quad (5)$$

so that distractors were added from the most similar available pathology profiles before more distant ones. The resulting hard-negative candidate pool was

$$\mathcal{R}_i^{(B)} = \{r_i\} \cup \mathcal{N}_i^{(B)}, \quad (6)$$

where $\mathcal{N}_i^{(B)}$ is formed from exact pathology matches followed by progressively less similar label vectors as needed. In the main experiments, Setting B was evaluated at $N = 10,000$, which served as the primary mechanistic operating point because it was large enough to approximate database-scale retrieval while still allowing clinically constrained distractor construction. Hard-negative candidate construction was repeated 10 times per query, and query-level performance was averaged across these repeated draws before final aggregation across the evaluation cohort.

The purpose of Setting A was to measure cross-modal linkage under increasingly large and otherwise unconstrained candidate pools. The purpose of Setting B was to test whether the retrieval signal persisted after suppressing broad disease-level shortcuts. Using both protocols allowed the study to separate simple label similarity from sharper instance-level image-report correspondence in the shared embedding space.

Head-only mitigation of the shared alignment layer

Mitigation was targeted at the final shared alignment layer rather than at the full multimodal backbone. The privacy risk studied here is mediated directly by the space in which chest radiographs and radiology reports are aligned for retrieval, so updating the entire model would have made it difficult to separate changes in cross-modal binding from broader changes in image or text representation. We therefore froze the pretrained BioViL-T image and text encoders and updated only the native image-side and text-side projection heads that map the two modalities into the shared retrieval space. No new projection architecture was introduced. This head-only setup contained 197,504 trainable parameters. BioViL-T was selected for mitigation because it showed the strongest linkage signal in the off-the-shelf analysis. All mitigation training was performed on the MIMIC-CXR training partition, and the resulting heads were then applied directly to CheXpert Plus without additional retraining.

Two projector-only mitigation variants were evaluated. The main method used differentially private finetuning of the projection heads with AdamW [35], learning rate 5×10^{-3} , weight decay 0.01, maximum per-sample gradient norm 1.5, and five training epochs. Privacy accounting was based on subsampling [12,27,10], so we report the nominal sampling size of 128, corresponding to a per-step sampling probability of $128/|\mathcal{D}_{\text{train}}|$. The privacy accountant used a fixed $\delta = 6 \times 10^{-6}$, which is smaller than the inverse of the AP/PA-filtered MIMIC-CXR training-set size after splitting ($1/153,255 \approx 6.53 \times 10^{-6}$). This is a standard DP choice because it keeps the allowed failure probability below the reciprocal of the training cohort size. The main reported checkpoint reached $\varepsilon = 0.34$. In practical terms, ε quantifies how much the distribution of the trained mechanism

can change when a single training example is added or removed: smaller values imply stronger privacy, and $\varepsilon = 0.34$ therefore represents a stringent guarantee for the projector-head training stage [12,10]. This guarantee applies only to the head-only finetuning procedure and not to the frozen pretrained backbone or to any data used before the private training stage.

As a non-private comparator, we also evaluated entropy-regularized head finetuning in the same frozen-backbone setting. This variant used the same 197,504 trainable parameters together with AdamW, learning rate 5×10^{-3} , and weight decay 0.01, but was trained without privacy noise, with a conventional batch size of 512, for 500 epochs. Because no privacy accountant was used in this setting, no ε value is defined for it. Matching the trainable modules and core optimization settings in the two variants ensured that differences in post-mitigation retrieval could be attributed to the mitigation strategy itself rather than to changes in architecture, backbone weights, or training data.

Cached-feature training pipeline and post-mitigation embedding construction

A full end-to-end private finetuning pipeline was not used. Because batch normalization [36] is not compatible with standard sample-wise privacy accounting [12,27,10,37], all batch normalization layers in the relevant BioViL-T modules were replaced with group normalization [38] using 32 groups, and in-place activations were also replaced with privacy-compatible alternatives where needed. The final mitigation pipeline therefore operated on cached frozen features. Let $f_{\text{img}}(\cdot)$ and $f_{\text{text}}(\cdot)$ denote the frozen image and text backbones, and let $g_{\text{img}}(\cdot; \theta_{\text{img}})$ and $g_{\text{text}}(\cdot; \theta_{\text{text}})$ denote the trainable image and text projection heads. For each paired example (x_i, r_i) , backbone features were first cached as $h_i^{\text{img}} = f_{\text{img}}(x_i)$ and $h_i^{\text{text}} = f_{\text{text}}(r_i)$, and only the projector parameters θ_{img} and θ_{text} were updated thereafter.

Projected embeddings were obtained from these cached features and normalized before loss computation:

$$u_i = \frac{g_{\text{img}}(h_i^{\text{img}}; \theta_{\text{img}})}{\|g_{\text{img}}(h_i^{\text{img}}; \theta_{\text{img}})\|_2}, \quad v_i = \frac{g_{\text{text}}(h_i^{\text{text}}; \theta_{\text{text}})}{\|g_{\text{text}}(h_i^{\text{text}}; \theta_{\text{text}})\|_2}. \quad (7)$$

With these normalized projector outputs, both mitigation variants retained the paired image-text contrastive objective that defines the shared retrieval space. For a batch of size B , the symmetric contrastive loss [39,40] was

$$\mathcal{L}_{\text{InfoNCE}} = \frac{1}{2B} \sum_{i=1}^B \left[-\log \frac{\exp(u_i^\top v_i / \tau)}{\sum_{j=1}^B \exp(u_i^\top v_j / \tau)} - \log \frac{\exp(v_i^\top u_i / \tau)}{\sum_{j=1}^B \exp(v_i^\top u_j / \tau)} \right], \quad (8)$$

where τ is the temperature parameter.

The DP variant optimized this projector-only contrastive objective under differentially private stochastic gradient descent (DP-SGD) [30]. For per-example loss ℓ_i , gradients were clipped to a maximum ℓ_2 norm C ,

$$\bar{g}_i = g_i \cdot \min\left(1, \frac{C}{\|g_i\|_2}\right), \quad (9)$$

and Gaussian noise was then added to the aggregated clipped gradient,

$$\tilde{g} = \frac{1}{B} \left(\sum_{i=1}^B \bar{g}_i + \mathcal{N}(0, \sigma^2 C^2 I) \right), \quad (10)$$

where σ is the noise multiplier. A Rényi DP accountant [41] was used to track cumulative privacy loss during optimization, with the main reported checkpoint corresponding to the $\delta = 6 \times 10^{-6}$,

$\varepsilon = 0.34$ setting described above. The entropy-regularized comparator used the same cached-feature projector-only pipeline but replaced the private optimizer with standard non-private optimization and augmented the contrastive loss with an entropy-style regularization term. If

$$p_{ij} = \frac{\exp(u_i^\top v_j / \tau)}{\sum_{k=1}^B \exp(u_i^\top v_k / \tau)}, \quad (11)$$

then the regularizer was

$$\mathcal{L}_{\text{bind}} = \sum_j p_{ij} \log p_{ij}, \quad (12)$$

and the final objective took the form

$$\mathcal{L} = \mathcal{L}_{\text{InfoNCE}} + \lambda \mathcal{L}_{\text{bind}}, \quad (13)$$

where λ controls the strength of the regularization.

Post-mitigation retrieval and utility evaluation were performed by reconstructing embeddings from cached test features and the saved projector weights rather than by rerunning the full BioViL-T model end to end. For each test example, final image and text embeddings were obtained as

$$\hat{z}_i^{\text{img}} = \frac{g_{\text{img}}(h_i^{\text{img}}; \hat{\theta}_{\text{img}})}{\|g_{\text{img}}(h_i^{\text{img}}; \hat{\theta}_{\text{img}})\|_2}, \quad \hat{z}_i^{\text{text}} = \frac{g_{\text{text}}(h_i^{\text{text}}; \hat{\theta}_{\text{text}})}{\|g_{\text{text}}(h_i^{\text{text}}; \hat{\theta}_{\text{text}})\|_2}, \quad (14)$$

where $\hat{\theta}_{\text{img}}$ and $\hat{\theta}_{\text{text}}$ denote the trained projector parameters. These projected embeddings were then passed through the same retrieval pipeline used for the off-the-shelf models, and the reconstructed image embeddings were also reused in the downstream image-only utility analysis.

Image-side utility evaluation

Image-side utility evaluated whether reducing cross-modal linkage weakened clinically useful image information. This analysis was intentionally image-only: once embeddings had been extracted, no report text was used. The downstream task was standard 14-label chest radiograph abnormality prediction. For the off-the-shelf model, fixed image embeddings were taken directly from the projected BioViL-T image representation used for retrieval. For the DP-mitigated model, embeddings were reconstructed by passing cached frozen image backbone features through the trained DP image projector and then ℓ_2 -normalizing the result, as in Eq. 14. These fixed embeddings were used as input to a linear probe for the 14 pathology labels. Let $e_i \in \mathbb{R}^d$ denote the embedding for example i . The probe was a single linear layer, $\hat{y}_i = W e_i + b$, where $W \in \mathbb{R}^{14 \times d}$ and $b \in \mathbb{R}^{14}$, followed by sigmoid activation. The primary utility endpoint was macro AUROC. Secondary utility metrics were macro accuracy, macro sensitivity, macro specificity, and their per-label counterparts. The main reported comparison focused on the off-the-shelf and DP-mitigated BioViL-T embeddings, because DP was the mitigation strategy that reduced linkage in the primary privacy analyses.

Statistical analysis

All analyses were performed in Python 3.11, including NumPy 1.26.4, pandas 3.0.0, SciPy 1.17.0, and scikit-learn 1.8.0. All retrieval and utility results were estimated with nonparametric bootstrap resampling using 1,000 redraws [42]. For retrieval analyses, the resampling unit was the query image. For utility analyses, the resampling unit was the held-out image example used in the linear-probe evaluation. Reported values correspond to the bootstrap mean, bootstrap standard deviation, and

95% confidence interval (CI) obtained from the bootstrap percentile distribution. All privacy and utility metrics were expressed in percentage form. Recall@1 was treated as the primary privacy endpoint, and macro area under the receiver operating characteristic curve (AUROC) was treated as the primary utility endpoint. For the utility comparison between off-the-shelf and DP-mitigated BioViL-T, formal two-sided paired bootstrap p-values were computed from the saved paired [43] bootstrap replicates [44]. No multiple-comparison correction was applied to these utility p-values.

Data availability

This study draws on publicly available datasets. MIMIC-CXR is distributed under controlled access via PhysioNet and requires completion of the corresponding data use agreements prior to download. Relevant dataset pages are available at <https://physionet.org/content/mimic-cxr-jpg/2.0.0/>. The CheXpert dataset and the extension CheXpert Plus are available upon request from Stanford University through <https://stanfordmlgroup.github.io/competitions/chexpert/> and <https://aimi.stanford.edu/datasets/chexpert-plus>.

Code availability

All source code, configuration files, and instructions required to reproduce the experiments in this study are publicly available at <https://github.com/tayebiarasteh/crossmodal>. All experiments reported in this work were performed on a Linux workstation equipped with a single NVIDIA L40S GPU with 48 GB VRAM and Intel Xeon Silver 4310 CPUs.

The implementation was developed in Python 3.11. The software environment used for the reported experiments included PyTorch 2.9.1+cu130, torchvision 0.24.1+cu130, transformers 5.0.0, accelerate 1.12.0, OpenCLIP 3.3.0, hi-ml-multimodal 0.2.2, Opacus 1.5.4 [45], NumPy 1.26.4, pandas 3.0.0, SciPy 1.17.0, scikit-learn 1.8.0, OpenCV 4.13.0.90, pydicom 3.0.2, SimpleITK 2.5.3, matplotlib 3.10.8, tokenizers 0.22.2, and Hugging Face Hub 1.3.4. All pretrained checkpoints were used in their released form without architectural modification of the backbones, except for the projector-head finetuning procedures described in the Methods. The evaluated checkpoints were loaded from their official public repositories:

- CLIP: <https://huggingface.co/openai/clip-vit-base-patch32>
- PubMedCLIP: <https://huggingface.co/flaviagammarino/pubmed-clip-vit-base-patch32>
- BiomedCLIP: https://huggingface.co/microsoft/BiomedCLIP-PubMedBERT_256-vit_base_patch16_224
- BioViL-T: <https://huggingface.co/microsoft/BiomedVLP-BioViL-T>

Acknowledgements

SN is supported by the Deutsche Forschungsgemeinschaft (DFG) (701010997, 517243167). DT is supported by the German Ministry of Research, Technology and Space (TRANSFORM LIVER - 031L0312C, DECIPHER-M - 01KD2420B), DFG (515639690), and the European Union (Horizon Europe, ODELIA - GA 101057091, ERC Starting Grant SAGMA – GA 101222556).

Author contributions

The formal analysis and conceptualization were conducted by STA and DT. The original draft was written by STA and edited by DT. The code was developed by STA and ML. The experiments

were performed by STA. The statistical analyses were performed by STA and DT. SN and DT provided clinical expertise. STA, ML, and DT provided technical expertise. The study was defined by STA. All authors read the manuscript, agreed to the submission of this paper, and contributed to the editing.

Declaration of interests

STA is on the editorial board of Communications Medicine and of European Radiology Experimental, and on the trainee editorial board of Radiology: Artificial Intelligence. ML is employed by Generali Deutschland Services GmbH, Germany, and is on the editorial board of European Radiology Experimental. DT received honoraria for lectures by Bayer, GE, Roche, AstraZeneca, and Philips and holds shares in StratifAI GmbH, Germany, and Synagen GmbH, Germany. The other authors declare no competing interests.

References

1. Lu, Y., Wang, A.: Integrating language into medical visual recognition and reasoning: A survey. *Medical Image Analysis* **102**, 103514 (2025). <https://doi.org/https://doi.org/10.1016/j.media.2025.103514>
2. Buess, L., Keicher, M., Navab, N., Maier, A., Tayebi Arasteh, S.: From large language models to multimodal ai: a scoping review on the potential of generative ai in medicine. *Biomedical Engineering Letters* **15**(5), 845–863 (2025)
3. Johnson, A.E., Pollard, T.J., Berkowitz, S.J., Greenbaum, N.R., Lungren, M.P., Deng, C.y., Mark, R.G., Horng, S.: Mimic-cxr, a de-identified publicly available database of chest radiographs with free-text reports. *Scientific data* **6**(1), 317 (2019)
4. Zhang, Y., Jiang, H., Miura, Y., Manning, C.D., Langlotz, C.P.: Contrastive learning of medical visual representations from paired images and text. In: Machine learning for healthcare conference. pp. 2–25. PMLR (2022)
5. Huang, S.C., Shen, L., Lungren, M.P., Yeung, S.: Gloria: A multimodal global-local representation learning framework for label-efficient medical image recognition. In: 2021 IEEE/CVF International Conference on Computer Vision (ICCV). pp. 3922–3931 (2021). <https://doi.org/10.1109/ICCV48922.2021.00391>
6. Bannur, S., Hyland, S., Liu, Q., Perez-Garcia, F., Ilse, M., Castro, D.C., Boecking, B., Sharma, H., Bouzid, K., Thieme, A., Schwaighofer, A., Wetscherek, M., Lungren, M.P., Nori, A., Alvarez-Valle, J., Oktay, O.: Learning to Exploit Temporal Structure for Biomedical Vision-Language Processing . In: 2023 IEEE/CVF Conference on Computer Vision and Pattern Recognition (CVPR). pp. 15016–15027. IEEE Computer Society, Los Alamitos, CA, USA (Jun 2023). <https://doi.org/10.1109/CVPR52729.2023.01442>
7. Goergen, S.K., Pool, F.J., Turner, T.J., Grimm, J.E., Appleyard, M.N., Crock, C., Fahey, M.C., Fay, M.F., Ferris, N.J., Liew, S.M., Perry, R.D., Revell, A., Russell, G.M., Wang, S.c.S., Wriedt, C.: Evidence-based guideline for the written radiology report: Methods, recommendations and implementation challenges. *Journal of Medical Imaging and Radiation Oncology* **57**(1), 1–7 (2013). <https://doi.org/https://doi.org/10.1111/1754-9485.12014>
8. Jain, S., Agrawal, A., Saporta, A., Truong, S., Duong, D.N., Bui, T., Chambon, P., Zhang, Y., Lungren, M.P., Ng, A.Y., Langlotz, C., Rajpurkar, P.: Radgraph: Extracting clinical entities and relations from radiology reports. In: Thirty-fifth Conference on Neural Information Processing Systems Datasets and Benchmarks Track (Round 1) (2021), <https://openreview.net/forum?id=pMwTc5NKd7V>
9. Truhn, D., Tayebi Arasteh, S., Saldanha, O.L., Müller-Franzes, G., Khader, F., Quirke, P., West, N.P., Gray, R., Hutchins, G.G., James, J.A., Loughrey, M.B., Salto-Tellez, M., Brenner, H., Brobeil, A., Yuan, T., Chang-Claude, J., Hoffmeister, M., Foersch, S., Han, T., Keil, S., Schulze-Hagen, M., Isfort, P., Bruners, P., Kaissis, G., Kuhl, C., Nebelung, S., Kather, J.N.: Encrypted federated learning for

- secure decentralized collaboration in cancer image analysis. *Medical Image Analysis* **92**, 103059 (2024). <https://doi.org/https://doi.org/10.1016/j.media.2023.103059>
10. Mohammadi, M., Vajdanihemmat, M., Lotfinia, M., Rusu, M., Truhn, D., Maier, A., Tayebi Arasteh, S.: Differential privacy for medical deep learning: methods, tradeoffs, and deployment implications. *npj Digital Medicine* **9**, 93 (2026)
 11. Dwork, C., Roth, A.: The algorithmic foundations of differential privacy. *foundations and trends® in theoretical computer science* **9** (3-4), 211–407 (2014)
 12. Tayebi Arasteh, S., Ziller, A., Kuhl, C., Makowski, M., Nebelung, S., Braren, R., Rueckert, D., Truhn, D., Kaissis, G.: Preserving fairness and diagnostic accuracy in private large-scale ai models for medical imaging. *Communications Medicine* **4**(1), 46 (2024)
 13. Ziller, A., Mueller, T.T., Stieger, S., Feiner, L.F., Brandt, J., Braren, R., Rueckert, D., Kaissis, G.: Reconciling privacy and accuracy in ai for medical imaging. *Nature Machine Intelligence* **6**(7), 764–774 (2024)
 14. Kaissis, G., Ziller, A., Passerat-Palmbach, J., Ryffel, T., Usynin, D., Trask, A., Lima Jr, I., Mancuso, J., Jungmann, F., Steinborn, M.M., et al.: End-to-end privacy preserving deep learning on multi-institutional medical imaging. *Nature Machine Intelligence* **3**(6), 473–484 (2021)
 15. Khader, F., Müller-Franzes, G., Wang, T., Han, T., Tayebi Arasteh, S., Haarbuerger, C., Stegmaier, J., Bressem, K., Kuhl, C., Nebelung, S., et al.: Multimodal deep learning for integrating chest radiographs and clinical parameters: a case for transformers. *Radiology* **309**(1), e230806 (2023)
 16. Arasteh, S.T., Joodaki, M., Lotfinia, M., Nebelung, S., Truhn, D.: Case-grounded evidence verification: A framework for constructing evidence-sensitive supervision. *arXiv preprint arXiv:2604.09537* (2026)
 17. Li, Y., Ghahremani, M., Wachinger, C.: Medbridge: Bridging foundation vision-language models to medical image diagnosis in chest x-ray. *arXiv preprint arXiv:2505.21698* (2025)
 18. Faghri, F., Fleet, D.J., Kiros, J.R., Fidler, S.: Vse++: Improving visual-semantic embeddings with hard negatives. *arXiv preprint arXiv:1707.05612* (2017)
 19. Radford, A., Kim, J.W., Hallacy, C., Ramesh, A., Goh, G., Agarwal, S., Sastry, G., Askell, A., Mishkin, P., Clark, J., Krueger, G., Sutskever, I.: Learning transferable visual models from natural language supervision. In: Meila, M., Zhang, T. (eds.) *Proceedings of the 38th International Conference on Machine Learning*. *Proceedings of Machine Learning Research*, vol. 139, pp. 8748–8763. PMLR (18–24 Jul 2021)
 20. Chambon, P., Delbrouck, J.B., Sounack, T., Huang, S.C., Chen, Z., Varma, M., Truong, S.Q., Chuong, C.T., Langlotz, C.P.: Chexpert plus: Augmenting a large chest x-ray dataset with text radiology reports, patient demographics and additional image formats (2024), <https://arxiv.org/abs/2405.19538>
 21. Irvin, J., Rajpurkar, P., Ko, M., Yu, Y., Ciurea-Ilcus, S., Chute, C., Marklund, H., Haghgoo, B., Ball, R., Shpanskaya, K., Seekins, J., Mong, D.A., Halabi, S.S., Sandberg, J.K., Jones, R., Larson, D.B., Langlotz, C.P., Patel, B.N., Lungren, M.P., Ng, A.Y.: Chexpert: a large chest radiograph dataset with uncertainty labels and expert comparison. In: *Proceedings of the Thirty-Third AAAI Conference on Artificial Intelligence and Thirty-First Innovative Applications of Artificial Intelligence Conference and Ninth AAAI Symposium on Educational Advances in Artificial Intelligence*. AAAI’19/IAAI’19/EAAI’19, AAAI Press (2019). <https://doi.org/10.1609/aaai.v33i01.3301590>
 22. Shannon, C.E.: A mathematical theory of communication. *The Bell system technical journal* **27**(3), 379–423 (1948)
 23. Chen, W., Shen, L., Lin, J., Luo, J., Li, X., Yuan, Y.: Fine-grained image-text alignment in medical imaging enables explainable cyclic image-report generation. In: *Proceedings of the 62nd Annual Meeting of the Association for Computational Linguistics (Volume 1: Long Papers)*. pp. 9494–9509. Association for Computational Linguistics, Bangkok, Thailand (2024). <https://doi.org/10.18653/v1/2024.acl-long.514>
 24. Zhang, S., Xu, Y., Usuyama, N., Xu, H., Bagga, J., Tinn, R., Preston, S., Rao, R., Wei, M., Valluri, N., Wong, C., Tupini, A., Wang, Y., Mazzola, M., Shukla, S., Liden, L., Gao, J., Crabtree, A., Piening, B., Bifulco, C., Lungren, M.P., Naumann, T., Wang, S., Poon, H.: A multimodal biomedical foundation model trained from fifteen million image–text pairs. *NEJM AI* **2**(1) (2024). <https://doi.org/10.1056/AIoa2400640>, <https://ai.nejm.org/doi/full/10.1056/AIoa2400640>

25. Kaissis, G.A., Makowski, M.R., Rückert, D., Braren, R.F.: Secure, privacy-preserving and federated machine learning in medical imaging. *Nature Machine Intelligence* **2**(6), 305–311 (2020)
26. Eslami, S., Meinel, C., de Melo, G.: PubMedCLIP: How much does CLIP benefit visual question answering in the medical domain? In: Vlachos, A., Augenstein, I. (eds.) *Findings of the Association for Computational Linguistics: EACL 2023*. pp. 1181–1193. Association for Computational Linguistics, Dubrovnik, Croatia (May 2023). <https://doi.org/10.18653/v1/2023.findings-eacl.88>
27. Tayebi Arasteh, S., Lotfinia, M., Nolte, T., Sähn, M.J., Isfort, P., Kuhl, C., Nebelung, S., Kaissis, G., Truhn, D.: Securing collaborative medical ai by using differential privacy: Domain transfer for classification of chest radiographs. *Radiology: Artificial Intelligence* **6**(1), e230212 (2023)
28. Wind, S., Nguyen, T.T., Sopa, J., Lotfinia, M., Bickelhaup, S., Uder, M., Köstler, H., Wellein, G., Nebelung, S., Truhn, D., Maier, A., Arasteh, S.T.: Safety and accuracy follow different scaling laws in clinical large language models (2026), <https://arxiv.org/abs/2605.04039>
29. Tayebi Arasteh, S., Truhn, D.: When framing shapes the answer: Cognitive bias and large language model reliability in radiology. *Radiology: Artificial Intelligence* **8**(3), e260346 (2026)
30. Abadi, M., Chu, A., Goodfellow, I., McMahan, H.B., Mironov, I., Talwar, K., Zhang, L.: Deep learning with differential privacy. In: *Proceedings of the 2016 ACM SIGSAC conference on computer and communications security*. pp. 308–318 (2016)
31. Tayebi Arasteh, S., Isfort, P., Saehn, M., Mueller-Franzes, G., Khader, F., Kather, J.N., Kuhl, C., Nebelung, S., Truhn, D.: Collaborative training of medical artificial intelligence models with non-uniform labels. *Scientific Reports* **13**(1), 6046 (2023)
32. Lotfinia, M., Tayebiarasteh, A., Samiei, S., Joodaki, M., Tayebi Arasteh, S.: Boosting multi-demographic federated learning for chest radiograph analysis using general-purpose self-supervised representations. *European Journal of Radiology Artificial Intelligence* **3**, 100028 (2025). <https://doi.org/https://doi.org/10.1016/j.ejrai.2025.100028>
33. Tayebi Arasteh, S., Misera, L., Kather, J.N., Truhn, D., Nebelung, S.: Enhancing diagnostic deep learning via self-supervised pretraining on large-scale, unlabeled non-medical images. *European Radiology Experimental* **8**(1), 10 (2024)
34. Sabottke, C.F., Spieler, B.M.: The effect of image resolution on deep learning in radiography. *Radiology: Artificial Intelligence* **2**(1), e190015 (2020)
35. Loshchilov, I., Hutter, F.: Decoupled weight decay regularization. In: *International Conference on Learning Representations (ICLR)* (2019), <https://openreview.net/forum?id=Bkg6RiCqY7>
36. Ioffe, S., Szegedy, C.: Batch normalization: Accelerating deep network training by reducing internal covariate shift. In: *International conference on machine learning (ICML)*. pp. 448–456. pmlr (2015)
37. Tayebi Arasteh, S., Lotfinia, M., Perez-Toro, P.A., Arias-Vergara, T., Ranji, M., Orozco-Aroyave, J.R., Schuster, M., Maier, A., Yang, S.H.: Differential privacy enables fair and accurate ai-based analysis of speech disorders while protecting patient data. *npj Artificial Intelligence* **1**(1), 37 (2025)
38. Wu, Y., He, K.: Group normalization. In: *Proceedings of the European conference on computer vision (ECCV)*. pp. 3–19 (2018)
39. Rusak, E., Reizinger, P., Juhos, A., Bringmann, O., Zimmermann, R.S., Brendel, W.: Infonce: Identifying the gap between theory and practice. In: Li, Y., Mandt, S., Agrawal, S., Khan, E. (eds.) *Proceedings of The 28th International Conference on Artificial Intelligence and Statistics. Proceedings of Machine Learning Research*, vol. 258, pp. 4159–4167. PMLR (03–05 May 2025), <https://proceedings.mlr.press/v258/rusak25a.html>
40. van den Oord, A., Li, Y., Vinyals, O.: Representation learning with contrastive predictive coding (2019), <https://arxiv.org/abs/1807.03748>
41. Mironov, I.: Rényi differential privacy. In: *2017 IEEE 30th computer security foundations symposium (CSF)*. pp. 263–275. IEEE (2017)
42. Tibshirani, R.J., Efron, B.: An introduction to the bootstrap. *Monographs on statistics and applied probability* **57**(1), 1–436 (1993)
43. Dietterich, T.G.: Approximate statistical tests for comparing supervised classification learning algorithms. *Neural computation* **10**(7), 1895–1923 (1998)
44. Konietzschke, F., Pauly, M.: Bootstrapping and permuting paired t-test type statistics. *Statistics and Computing* **24**(3), 283–296 (2014)

45. Yousefpour, A., Shilov, I., Sablayrolles, A., Testuggine, D., Prasad, K., Malek, M., Nguyen, J., Ghosh, S., Bharadwaj, A., Zhao, J., Cormode, G., Mironov, I.: Opacus: User-friendly differential privacy library in PyTorch. In: NeurIPS Workshop on Privacy in Machine Learning (2021)

Supplementary information

Supplementary Table 1: Full retrieval results on MIMIC-CXR under the random-candidate setting. For each query chest radiograph on the MIMIC-CXR test set, the paired radiology report is retrieved from a candidate pool sampled from the held-out test split. Values are reported in percent as mean \pm standard deviation with corresponding 95% confidence intervals.

N	Model	Statistic	Recall@1	Recall@5	Recall@10	MRR	
100	BioViL-T	Mean \pm SD	15.440 \pm 0.141	41.896 \pm 0.223	58.673 \pm 0.225	28.936 \pm 0.152	
		95% CI	[15.181, 15.706]	[41.491, 42.334]	[58.252, 59.116]	[28.655, 29.233]	
	BiomedCLIP	Mean \pm SD	5.829 \pm 0.091	19.987 \pm 0.173	31.709 \pm 0.203	14.523 \pm 0.109	
		95% CI	[5.647, 6.001]	[19.649, 20.344]	[31.316, 32.158]	[14.298, 14.734]	
	PubMedCLIP	Mean \pm SD	1.594 \pm 0.046	6.316 \pm 0.104	11.787 \pm 0.140	6.113 \pm 0.062	
		95% CI	[1.506, 1.684]	[6.120, 6.518]	[11.504, 12.055]	[5.997, 6.237]	
	CLIP	Mean \pm SD	1.203 \pm 0.035	5.917 \pm 0.092	11.346 \pm 0.127	5.674 \pm 0.052	
		95% CI	[1.136, 1.273]	[5.739, 6.093]	[11.106, 11.588]	[5.574, 5.780]	
	Random	Mean \pm SD	1.000 \pm 0.000	5.000 \pm 0.000	10.000 \pm 0.000	5.187 \pm 0.000	
		95% CI	[1.000, 1.000]	[5.000, 5.000]	[10.000, 10.000]	[5.187, 5.187]	
	1,000	BioViL-T	Mean \pm SD	3.320 \pm 0.065	11.197 \pm 0.140	17.723 \pm 0.180	8.407 \pm 0.087
			95% CI	[3.198, 3.448]	[10.921, 11.470]	[17.391, 18.055]	[8.242, 8.580]
BiomedCLIP		Mean \pm SD	0.997 \pm 0.039	3.772 \pm 0.086	6.330 \pm 0.114	3.235 \pm 0.054	
		95% CI	[0.926, 1.074]	[3.589, 3.936]	[6.096, 6.548]	[3.128, 3.335]	
PubMedCLIP		Mean \pm SD	0.213 \pm 0.016	0.873 \pm 0.038	1.549 \pm 0.054	1.031 \pm 0.024	
		95% CI	[0.183, 0.244]	[0.799, 0.947]	[1.442, 1.658]	[0.986, 1.080]	
CLIP		Mean \pm SD	0.134 \pm 0.013	0.603 \pm 0.031	1.197 \pm 0.046	0.849 \pm 0.019	
		95% CI	[0.110, 0.158]	[0.541, 0.662]	[1.106, 1.290]	[0.814, 0.886]	
Random		Mean \pm SD	0.100 \pm 0.000	0.500 \pm 0.000	1.000 \pm 0.000	0.749 \pm 0.000	
		95% CI	[0.100, 0.100]	[0.500, 0.500]	[1.000, 1.000]	[0.749, 0.749]	
10,000		BioViL-T	Mean \pm SD	0.496 \pm 0.027	2.040 \pm 0.060	3.642 \pm 0.083	1.790 \pm 0.037
			95% CI	[0.445, 0.551]	[1.926, 2.163]	[3.478, 3.808]	[1.718, 1.863]
	BiomedCLIP	Mean \pm SD	0.137 \pm 0.015	0.613 \pm 0.035	1.118 \pm 0.051	0.604 \pm 0.021	
		95% CI	[0.110, 0.168]	[0.546, 0.681]	[1.025, 1.222]	[0.565, 0.647]	
	PubMedCLIP	Mean \pm SD	0.024 \pm 0.006	0.112 \pm 0.014	0.206 \pm 0.020	0.152 \pm 0.008	
		95% CI	[0.013, 0.035]	[0.087, 0.141]	[0.170, 0.246]	[0.136, 0.170]	
	CLIP	Mean \pm SD	0.014 \pm 0.004	0.098 \pm 0.013	0.161 \pm 0.018	0.125 \pm 0.007	
		95% CI	[0.007, 0.022]	[0.073, 0.125]	[0.128, 0.198]	[0.112, 0.138]	
	Random	Mean \pm SD	0.010 \pm 0.000	0.050 \pm 0.000	0.100 \pm 0.000	0.098 \pm 0.000	
		95% CI	[0.010, 0.010]	[0.050, 0.050]	[0.100, 0.100]	[0.098, 0.098]	
	43,793	BioViL-T	Mean \pm SD	0.150 \pm 0.019	0.570 \pm 0.036	1.037 \pm 0.049	0.602 \pm 0.022
			95% CI	[0.117, 0.190]	[0.502, 0.644]	[0.941, 1.133]	[0.559, 0.647]
BiomedCLIP		Mean \pm SD	0.041 \pm 0.010	0.167 \pm 0.020	0.281 \pm 0.026	0.191 \pm 0.012	
		95% CI	[0.023, 0.062]	[0.128, 0.208]	[0.233, 0.331]	[0.168, 0.216]	
PubMedCLIP		Mean \pm SD	0.005 \pm 0.003	0.028 \pm 0.008	0.048 \pm 0.011	0.041 \pm 0.004	
		95% CI	[0.000, 0.011]	[0.014, 0.043]	[0.030, 0.071]	[0.034, 0.050]	
CLIP		Mean \pm SD	0.002 \pm 0.002	0.012 \pm 0.005	0.036 \pm 0.009	0.032 \pm 0.003	
		95% CI	[0.000, 0.007]	[0.002, 0.023]	[0.021, 0.055]	[0.027, 0.039]	
Random		Mean \pm SD	0.002 \pm 0.000	0.011 \pm 0.000	0.023 \pm 0.000	0.026 \pm 0.000	
		95% CI	[0.002, 0.002]	[0.011, 0.011]	[0.023, 0.023]	[0.026, 0.026]	

Supplementary Table 2: Full retrieval results on CheXpert Plus under the random-candidate setting. For each query chest radiograph on the CheXpert Plus test set, the paired radiology report is retrieved from a candidate pool sampled from the held-out test split. Values are reported in percent as mean \pm standard deviation with corresponding 95% confidence intervals.

N	Model	Statistic	Recall@1	Recall@5	Recall@10	MRR
100	BioViL-T	Mean \pm SD	7.281 \pm 0.114	25.063 \pm 0.220	39.423 \pm 0.256	17.628 \pm 0.136
		95% CI	[7.065, 7.508]	[24.618, 25.497]	[38.929, 39.916]	[17.367, 17.905]
	BiomedCLIP	Mean \pm SD	5.456 \pm 0.100	18.270 \pm 0.196	29.478 \pm 0.234	13.684 \pm 0.123
		95% CI	[5.261, 5.657]	[17.865, 18.657]	[29.000, 29.930]	[13.429, 13.921]
	PubMedCLIP	Mean \pm SD	1.179 \pm 0.047	5.784 \pm 0.123	11.425 \pm 0.172	5.715 \pm 0.069
		95% CI	[1.087, 1.273]	[5.535, 6.018]	[11.099, 11.771]	[5.580, 5.853]
	CLIP	Mean \pm SD	0.928 \pm 0.040	5.011 \pm 0.111	10.428 \pm 0.166	5.218 \pm 0.060
		95% CI	[0.850, 1.008]	[4.798, 5.228]	[10.088, 10.753]	[5.103, 5.336]
	Random	Mean \pm SD	1.000 \pm 0.000	5.000 \pm 0.000	10.000 \pm 0.000	5.187 \pm 0.000
		95% CI	[1.000, 1.000]	[5.000, 5.000]	[10.000, 10.000]	[5.187, 5.187]
1,000	BioViL-T	Mean \pm SD	1.202 \pm 0.047	4.737 \pm 0.111	8.141 \pm 0.146	4.019 \pm 0.067
		95% CI	[1.110, 1.296]	[4.518, 4.963]	[7.862, 8.428]	[3.885, 4.151]
	BiomedCLIP	Mean \pm SD	0.914 \pm 0.043	3.389 \pm 0.094	5.885 \pm 0.129	3.013 \pm 0.059
		95% CI	[0.834, 1.003]	[3.214, 3.573]	[5.639, 6.137]	[2.905, 3.129]
	PubMedCLIP	Mean \pm SD	0.154 \pm 0.018	0.668 \pm 0.044	1.276 \pm 0.063	0.915 \pm 0.027
		95% CI	[0.119, 0.189]	[0.584, 0.758]	[1.151, 1.406]	[0.861, 0.970]
	CLIP	Mean \pm SD	0.141 \pm 0.016	0.655 \pm 0.041	1.241 \pm 0.059	0.876 \pm 0.024
		95% CI	[0.109, 0.172]	[0.575, 0.734]	[1.127, 1.358]	[0.827, 0.925]
	Random	Mean \pm SD	0.100 \pm 0.000	0.500 \pm 0.000	1.000 \pm 0.000	0.749 \pm 0.000
		95% CI	[0.100, 0.100]	[0.500, 0.500]	[1.000, 1.000]	[0.749, 0.749]
10,000	BioViL-T	Mean \pm SD	0.153 \pm 0.018	0.697 \pm 0.042	1.311 \pm 0.061	0.726 \pm 0.026
		95% CI	[0.121, 0.192]	[0.617, 0.785]	[1.197, 1.433]	[0.678, 0.780]
	BiomedCLIP	Mean \pm SD	0.124 \pm 0.016	0.555 \pm 0.040	0.983 \pm 0.055	0.555 \pm 0.024
		95% CI	[0.093, 0.155]	[0.480, 0.634]	[0.876, 1.093]	[0.509, 0.602]
	PubMedCLIP	Mean \pm SD	0.020 \pm 0.007	0.078 \pm 0.015	0.160 \pm 0.023	0.130 \pm 0.010
		95% CI	[0.007, 0.035]	[0.049, 0.106]	[0.116, 0.204]	[0.111, 0.150]
	CLIP	Mean \pm SD	0.011 \pm 0.005	0.063 \pm 0.013	0.131 \pm 0.019	0.114 \pm 0.007
		95% CI	[0.003, 0.021]	[0.039, 0.089]	[0.095, 0.170]	[0.100, 0.130]
	Random	Mean \pm SD	0.010 \pm 0.000	0.050 \pm 0.000	0.100 \pm 0.000	0.098 \pm 0.000
		95% CI	[0.010, 0.010]	[0.050, 0.050]	[0.100, 0.100]	[0.098, 0.098]
29,296	BioViL-T	Mean \pm SD	0.048 \pm 0.013	0.243 \pm 0.028	0.486 \pm 0.040	0.305 \pm 0.017
		95% CI	[0.027, 0.075]	[0.191, 0.300]	[0.410, 0.567]	[0.275, 0.339]
	BiomedCLIP	Mean \pm SD	0.044 \pm 0.013	0.201 \pm 0.026	0.402 \pm 0.037	0.237 \pm 0.016
		95% CI	[0.021, 0.072]	[0.150, 0.253]	[0.331, 0.478]	[0.208, 0.271]
	PubMedCLIP	Mean \pm SD	0.010 \pm 0.006	0.037 \pm 0.012	0.051 \pm 0.014	0.054 \pm 0.007
		95% CI	[0.000, 0.024]	[0.014, 0.061]	[0.024, 0.079]	[0.041, 0.069]
	CLIP	Mean \pm SD	0.003 \pm 0.003	0.024 \pm 0.009	0.048 \pm 0.013	0.044 \pm 0.004
		95% CI	[0.000, 0.010]	[0.007, 0.041]	[0.027, 0.075]	[0.036, 0.054]
	Random	Mean \pm SD	0.003 \pm 0.000	0.017 \pm 0.000	0.034 \pm 0.000	0.037 \pm 0.000
		95% CI	[0.003, 0.003]	[0.017, 0.017]	[0.034, 0.034]	[0.037, 0.037]

Supplementary Table 3: Full per-label utility after mitigation. Per-label diagnostic utility of BioViL-T image embeddings before and after DP mitigation on the MIMIC-CXR test set. Utility was assessed with image-only linear probing on the 14 pathology labels. Metrics include AUROC, accuracy, sensitivity, and specificity. Values are reported in percent as mean \pm standard deviation with corresponding 95% confidence intervals, computed using 1,000 bootstrap resamples over test images.

Label	Method	Statistic	AUROC	Accuracy	Sensitivity	Specificity
Atelectasis	Off-the-shelf	Mean \pm SD	80.03 \pm 0.24	80.72 \pm 0.19	20.73 \pm 0.43	95.64 \pm 0.10
		95% CI	[79.56, 80.49]	[80.35, 81.06]	[19.87, 21.57]	[95.43, 95.84]
	DP	Mean \pm SD	79.88 \pm 0.24	80.86 \pm 0.19	22.80 \pm 0.47	95.30 \pm 0.11
		95% CI	[79.41, 80.34]	[80.48, 81.24]	[21.89, 23.74]	[95.07, 95.50]
Cardiomegaly	Off-the-shelf	Mean \pm SD	80.53 \pm 0.23	80.32 \pm 0.19	24.08 \pm 0.45	95.16 \pm 0.11
		95% CI	[80.06, 80.98]	[79.98, 80.69]	[23.20, 24.96]	[94.94, 95.38]
	DP	Mean \pm SD	80.17 \pm 0.24	80.34 \pm 0.19	24.12 \pm 0.46	95.17 \pm 0.11
		95% CI	[79.69, 80.64]	[79.98, 80.73]	[23.25, 25.03]	[94.95, 95.39]
Consolidation	Off-the-shelf	Mean \pm SD	80.57 \pm 0.47	96.01 \pm 0.09	0.06 \pm 0.06	100.00 \pm 0.00
		95% CI	[79.59, 81.51]	[95.83, 96.18]	[0.00, 0.18]	[99.99, 100.00]
	DP	Mean \pm SD	80.26 \pm 0.47	96.00 \pm 0.09	0.06 \pm 0.06	99.99 \pm 0.00
		95% CI	[79.29, 81.20]	[95.83, 96.17]	[0.00, 0.18]	[99.98, 100.00]
Edema	Off-the-shelf	Mean \pm SD	88.89 \pm 0.20	88.55 \pm 0.15	33.81 \pm 0.67	96.74 \pm 0.09
		95% CI	[88.50, 89.27]	[88.25, 88.84]	[32.49, 35.07]	[96.55, 96.93]
	DP	Mean \pm SD	88.71 \pm 0.20	88.57 \pm 0.15	34.19 \pm 0.65	96.71 \pm 0.09
		95% CI	[88.33, 89.11]	[88.28, 88.86]	[32.90, 35.48]	[96.53, 96.88]
Enlarged cardiome-diastinum	Off-the-shelf	Mean \pm SD	72.28 \pm 0.62	96.95 \pm 0.09	0.00 \pm 0.00	100.00 \pm 0.00
		95% CI	[71.08, 73.53]	[96.79, 97.12]	[0.00, 0.00]	[100.00, 100.00]
	DP	Mean \pm SD	71.51 \pm 0.63	96.95 \pm 0.09	0.00 \pm 0.00	100.00 \pm 0.00
		95% CI	[70.27, 72.73]	[96.79, 97.12]	[0.00, 0.00]	[100.00, 100.00]
Fracture	Off-the-shelf	Mean \pm SD	64.78 \pm 0.86	97.96 \pm 0.06	0.00 \pm 0.00	100.00 \pm 0.00
		95% CI	[63.13, 66.45]	[97.84, 98.08]	[0.00, 0.00]	[100.00, 100.00]
	DP	Mean \pm SD	65.20 \pm 0.89	97.96 \pm 0.06	0.00 \pm 0.00	100.00 \pm 0.00
		95% CI	[63.45, 66.87]	[97.84, 98.08]	[0.00, 0.00]	[100.00, 100.00]
Lung lesion	Off-the-shelf	Mean \pm SD	74.29 \pm 0.73	97.42 \pm 0.08	0.00 \pm 0.00	100.00 \pm 0.00
		95% CI	[72.84, 75.73]	[97.27, 97.57]	[0.00, 0.00]	[100.00, 100.00]
	DP	Mean \pm SD	73.86 \pm 0.73	97.41 \pm 0.08	0.08 \pm 0.09	99.99 \pm 0.00
		95% CI	[72.46, 75.29]	[97.27, 97.56]	[0.00, 0.27]	[99.98, 100.00]
Lung opacity	Off-the-shelf	Mean \pm SD	75.77 \pm 0.28	81.12 \pm 0.19	12.27 \pm 0.36	97.65 \pm 0.08
		95% CI	[75.24, 76.32]	[80.74, 81.48]	[11.56, 12.99]	[97.48, 97.80]
	DP	Mean \pm SD	75.81 \pm 0.27	81.07 \pm 0.19	9.18 \pm 0.31	98.33 \pm 0.07
		95% CI	[75.27, 76.33]	[80.70, 81.43]	[8.59, 9.77]	[98.19, 98.46]
Pleural effusion	Off-the-shelf	Mean \pm SD	88.81 \pm 0.17	84.36 \pm 0.16	54.57 \pm 0.48	93.40 \pm 0.13
		95% CI	[88.48, 89.16]	[84.05, 84.67]	[53.62, 55.54]	[93.14, 93.67]
	DP	Mean \pm SD	88.54 \pm 0.18	84.12 \pm 0.17	55.32 \pm 0.48	92.87 \pm 0.14
		95% CI	[88.19, 88.88]	[83.78, 84.43]	[54.38, 56.22]	[92.60, 93.14]
Pleural other	Off-the-shelf	Mean \pm SD	82.81 \pm 0.99	99.01 \pm 0.04	0.00 \pm 0.00	100.00 \pm 0.00
		95% CI	[80.81, 84.69]	[98.92, 99.10]	[0.00, 0.00]	[100.00, 100.00]
	DP	Mean \pm SD	82.10 \pm 0.94	99.01 \pm 0.04	0.00 \pm 0.00	100.00 \pm 0.00
		95% CI	[80.25, 84.01]	[98.92, 99.10]	[0.00, 0.00]	[100.00, 100.00]
Pneumonia	Off-the-shelf	Mean \pm SD	74.18 \pm 0.48	93.06 \pm 0.13	1.12 \pm 0.20	99.93 \pm 0.01
		95% CI	[73.23, 75.08]	[92.80, 93.31]	[0.73, 1.52]	[99.91, 99.96]
	DP	Mean \pm SD	73.90 \pm 0.48	93.06 \pm 0.13	1.09 \pm 0.19	99.94 \pm 0.01
		95% CI	[72.92, 74.79]	[92.80, 93.31]	[0.73, 1.47]	[99.92, 99.96]
Pneumothorax	Off-the-shelf	Mean \pm SD	80.59 \pm 0.48	95.49 \pm 0.10	0.76 \pm 0.20	99.96 \pm 0.01
		95% CI	[79.59, 81.52]	[95.30, 95.67]	[0.39, 1.14]	[99.94, 99.98]
	DP	Mean \pm SD	80.86 \pm 0.49	95.58 \pm 0.10	4.40 \pm 0.45	99.89 \pm 0.02
		95% CI	[79.84, 81.80]	[95.40, 95.78]	[3.55, 5.27]	[99.85, 99.92]
Support devices	Off-the-shelf	Mean \pm SD	87.05 \pm 0.18	81.70 \pm 0.19	61.19 \pm 0.42	90.13 \pm 0.17
		95% CI	[86.69, 87.40]	[81.32, 82.07]	[60.36, 62.03]	[89.79, 90.46]
	DP	Mean \pm SD	86.98 \pm 0.18	81.49 \pm 0.18	59.55 \pm 0.43	90.51 \pm 0.16
		95% CI	[86.61, 87.33]	[81.14, 81.85]	[58.67, 60.35]	[90.19, 90.82]
No finding	Off-the-shelf	Mean \pm SD	84.25 \pm 0.19	78.86 \pm 0.19	63.61 \pm 0.38	87.68 \pm 0.20
		95% CI	[83.87, 84.64]	[78.49, 79.24]	[62.92, 64.34]	[87.30, 88.08]
	DP	Mean \pm SD	84.23 \pm 0.19	78.82 \pm 0.19	65.68 \pm 0.37	86.41 \pm 0.20
		95% CI	[83.88, 84.62]	[78.47, 79.19]	[64.96, 66.44]	[86.01, 86.79]
Macro average	Off-the-shelf	Mean \pm SD	79.63 \pm 0.15	89.39 \pm 0.04	19.44 \pm 0.09	96.88 \pm 0.03
		95% CI	[79.32, 79.90]	[89.31, 89.48]	[19.25, 19.62]	[96.83, 96.93]
	DP	Mean \pm SD	79.43 \pm 0.15	89.37 \pm 0.04	19.75 \pm 0.10	96.79 \pm 0.03
		95% CI	[79.13, 79.72]	[89.29, 89.46]	[19.56, 19.95]	[96.74, 96.84]

Supplementary Table 4: Label prevalence across splits. Prevalence of the 14 pathology labels used for hard-negative construction and image-only utility evaluation. Labels follow the study convention in which uncertain values are mapped according to the final training convention and missing labels are masked in supervised utility training. MIMIC-CXR values below were calculated from the finalized AP/PA-filtered split file.

Dataset	Label	Training (%)	Validation (%)	Test (%)
MIMIC-CXR	Atelectasis	19.89	19.60	19.92
	Cardiomegaly	19.48	19.80	20.62
	Consolidation	4.03	3.73	3.99
	Edema	11.25	11.18	12.32
	Enlarged cardiomeastinum	3.03	2.98	3.05
	Fracture	1.89	1.78	2.03
	Lung lesion	2.62	2.78	2.57
	Lung opacity	19.05	18.35	19.09
	No finding	37.90	38.51	36.64
	Pleural effusion	22.44	22.74	23.29
	Pleural other	0.77	0.78	0.99
	Pneumonia	6.48	6.17	6.53
	Pneumothorax	4.61	4.56	4.51
	Support devices	28.48	27.43	29.09
CheXpert Plus	Atelectasis	16.88	17.58	15.42
	Cardiomegaly	12.40	12.44	13.45
	Consolidation	5.99	6.41	6.08
	Edema	27.87	28.47	24.91
	Enlarged cardiomeastinum	4.88	5.86	4.72
	Fracture	4.02	3.74	4.48
	Lung lesion	3.68	3.76	3.71
	Lung opacity	47.56	47.08	43.93
	No finding	10.47	10.47	12.07
	Pleural effusion	41.96	40.20	39.00
	Pleural other	1.20	1.18	1.68
	Pneumonia	2.47	2.27	2.78
	Pneumothorax	10.03	11.22	11.03
	Support devices	58.61	58.19	53.46

Supplementary Table 5: Model implementation details. Implementation details for the evaluated off-the-shelf vision-language models. Retrieval-space dimension refers to the final embedding space used for image-to-report cosine-similarity ranking.

Characteristic	CLIP	PubMedCLIP	BiomedCLIP	BioViL-T
Input image size	224	224	224	224
Text truncation length	77	77	256	512
Raw embedding dimension	768 / 512	768 / 512	768	768
Retrieval-space dimension	512	512	512	128
Loading interface	Hugging Face	Hugging Face	OpenCLIP	health_multimodal